ADVANCING EARTH AND SPACE SCIENCES

JGR Atmospheres

RESEARCH ARTICLE
10.1029/2025JD046293

Key Points:

- Including sub-grid turbulent orographic form drag (STOFD) improves wind and precipitation simulations with distinct seasonal differences
- The STOFD triggers a meridional circulation and pressure differences by impeding westerlies to reshape the circulation and precipitation
- The seasonal variations of the intensity and location of background westerlies collectively determine the seasonality of STOFD's impacts

Correspondence to:
A. Huang and C. Gu,
anhuang@nju.edu.cn;
chlgu@nju.edu.cn

Citation:
Zhou, Y., Huang, A., Gu, C., Li, X., & Wu, Y. (2026). Seasonal difference in the impact of sub-grid turbulent orographic form drag scheme on the simulations of winds and precipitation over China. *Journal of Geophysical Research: Atmospheres*, *131*, e2025JD046293. https://doi.org/10.1029/2025JD046293

Received 31 DEC 2025
Accepted 23 JUL 2026

Author Contributions:
Conceptualization: Anning Huang
Data curation: Yuchen Zhou, Chunlei Gu
Formal analysis: Yuchen Zhou
Investigation: Yuchen Zhou, Anning Huang, Chunlei Gu, Xin Li, Yang Wu
Methodology: Yuchen Zhou, Chunlei Gu
Resources: Chunlei Gu, Xin Li
Software: Yuchen Zhou
Supervision: Anning Huang, Chunlei Gu
Validation: Yuchen Zhou
Visualization: Yuchen Zhou
Writing – original draft: Yuchen Zhou, Anning Huang, Chunlei Gu, Xin Li, Yang Wu
Writing – review & editing: Yuchen Zhou, Anning Huang, Chunlei Gu, Xin Li, Yang Wu

Seasonal Difference in the Impact of Sub-Grid Turbulent Orographic Form Drag Scheme on the Simulations of Winds and Precipitation Over China

Yuchen Zhou[1], Anning Huang[1,2], Chunlei Gu[1], Xin Li[3], and Yang Wu[3]

[1]School of Atmospheric Sciences, Nanjing University, Nanjing, China, [2]Qinghai Lake Comprehensive Observation Research Station, Chinese Academy of Sciences, Gangcha, China, [3]Key Laboratory of Transportation Meteorology of China Meteorological Administration, Nanjing Joint Institute for Atmospheric Sciences, Nanjing, China

Abstract This study systematically evaluates the influence of the sub-grid turbulent orographic form drag (STOFD) scheme on the performance of the Regional Climate Model Version 4 in simulating 10 m wind and precipitation over China across seasons and investigates underlying mechanisms. Results demonstrate that the improvement of 10 m wind simulation across China induced by STOFD scheme is the most pronounced in winter among all seasons, reducing root mean square error (RMSE) by 27.72% and increasing Taylor score by 46.09% for wind speed, with improvement degree positively correlated with micro-scale terrain complexity. The effects of STOFD scheme on precipitation simulations also vary seasonally. Specifically, adopting STOFD scheme most effectively reduces precipitation overestimation over the Tibetan Plateau in winter among all seasons, with RMSE reduced by 9.69%. The greatest improvements in precipitation simulations over the Southeastern and Northeastern China occur in summer among all seasons, with RMSE reductions of 6.45% and 33.11%, respectively. Mechanistically, STOFD impedes westerlies, generating southeasterly wind differences that trigger secondary meridional circulation and pressure differences, enhancing westerlies on both sides of the southeasterly wind differences and inducing cyclonic (anticyclonic) differences over the Southeastern (Northeastern) China. Seasonal variations in the intensity and position of background westerlies modulate the magnitude and distribution of STOFD-induced 10 m wind simulation improvements, thereby driving the seasonality of impacts on regional circulation and water vapor transport, shaping clear seasonal differences in improvements of precipitation simulations. This study reveals seasonality in the effects of STOFD scheme, offering crucial insights for model development.

Plain Language Summary The sub-grid turbulent orographic form drag (STOFD) describes the dissipation of momentum caused by the interaction between airflow and unresolved micro-scale terrain. Although prior research has recognized the climatic effects of the STOFD scheme in model simulations, the seasonal difference of these influences has not been systematically examined. This study addresses this gap through a 5-year continuous regional climate simulation over China using the Regional Climate Model Version 4. Results reveal that the STOFD-induced improvement of 10 m wind simulations across China in winter is the most notable among all seasons, while the most significant improvement in precipitation simulations induced by the STOFD occurs over the Tibetan Plateau in winter and eastern China in summer among all seasons. Seasonal variations in intensity and location of the background westerlies collectively govern the magnitude and direction of STOFD, thereby differentially modifying the simulations of 10 m wind, circulation, water vapor transport, and precipitation in various seasons. This study advances the understanding of the seasonal differences in the impact of STOFD on the performance of regional climate simulations.

1. Introduction

With the rapid growth of the low-altitude economy, the urgent demand for precise simulation and forecast of near-surface wind and precipitation has continued to rise (Huang et al., 2024; Ilyas et al., 2025; Lee et al., 2022; Qin et al., 2025). The performance of the near-surface wind and precipitation simulations is governed by multiple factors, such as model resolution, terrain representation, and the parameterization of physical processes (Andrade Cardoso et al., 2025; Namdev et al., 2024; Park et al., 2024; Xu et al., 2023). Since the scale of real terrain is much finer than the resolution of model grids, the resulting unrepresented sub-grid terrain becomes a major source of simulation deviation (Cannon et al., 2017; Sandu et al., 2019; Wang et al., 2023).

The effects generated by sub-grid terrain on the airflow need to be characterized through parameterization schemes (Niekerk et al., 2016; Zuo & Wu, 2025). Numerous sub-grid terrain parameterization schemes have been developed and implemented in numerical models, demonstrating consistent improvements in simulation and prediction accuracy across diverse regions and applications (Elvidge et al., 2019; Wang & Wu, 2022). For example, the application of a three-dimensional sub-grid terrain solar radiative scheme mitigates the precipitation overestimation over the southern Tibetan Plateau (TP) by reducing surface solar radiation, weakening plateau thermal forcing, enhancing atmospheric stability, and diminishing southwesterly moisture transport (Cai et al., 2023).

The sub-grid turbulent orographic form drag (STOFD) is generated by the uneven pressure distribution on the windward and leeward slopes of the sub-grid micro-scale terrain (Belcher et al., 1993). The parameterization scheme of STOFD is widely recognized for its substantial impact on the 10 m wind simulations (Gu et al., 2022; Koo et al., 2018; Xu et al., 2023; X. Zhou et al., 2017). Compared to flow blocking drag and orographic gravity wave drag parameterization schemes, the STOFD scheme has proven to be the most critical for improving 10 m wind simulations (Xu et al., 2023; Zuo & Wu, 2025). Consequently, numerous studies have investigated the effect of the STOFD parameterization schemes on the near-surface wind simulations (Xue & Shen, 2023; Xue et al., 2021; X. Zhou et al., 2018). For instance, the STOFD scheme substantially improves 10 m wind simulations over the western TP in winter by reducing the wind speed overestimation and correcting the diurnal phase of the zonal wind (X. Zhou et al., 2019). It can not only significantly improve the 10 m wind simulations, but also indirectly regulate the precipitation simulations by influencing water vapor transport and ascending motion (J. Li et al., 2024; Wang et al., 2020; Y. Zhou et al., 2024). The STOFD scheme alters the precipitation distribution in the Central Himalayas with more precipitation in the lowlands and less precipitation at high altitudes by slowing the winds and hindering the moisture uplift (Wang et al., 2020).

Previous studies have predominantly focused on single-season analysis, exploring the impact of the STOFD scheme on the 10 m wind and precipitation simulations in specific seasons, while the seasonal differences of improvements and underlying mechanisms have been poorly explored (Gu et al., 2023a; Wang et al., 2020; X. Zhou et al., 2019). The enhanced intensity of the STOFD can rapidly induce deceleration of surface westerlies and meridional pressure gradient adjustments, subsequently altering zonal wind, temperature, and geopotential height across all time scales in winter (Sandu et al., 2016). In southern China, the impact of the STOFD scheme weakens the simulated 10 m and low-level winds, suppressing the southwesterlies and promoting low-level moisture convergence, which consequently increases the simulated rainfall in pre-summer (Xue et al., 2021).

The impact of the STOFD scheme on simulated precipitation varies seasonally, with a reduction in winter over TP but an enhancement in summer (Gu et al., 2023a; X. Zhou et al., 2019). However, these studies employ different models and simulation domains, making it impossible to attribute the seasonal contrast solely to a seasonal difference in the impacts of the STOFD scheme. A systematic investigation of the seasonality in the impacts of the STOFD scheme, ideally within a consistent modeling framework, is therefore urgently needed.

The systematic investigation of the seasonality in the impacts of the STOFD scheme is particularly critical in regions like China with distinctly different climate systems across seasons. The seasonal variations in the westerlies over the mid-latitudes, the East Asian monsoon, and other associated factors collectively establish distinct dynamic backgrounds in various seasons (Asakereh & Jahedi, 2025; Curio & Scherer, 2016; Yihui & Chan, 2005). Moreover, substantial evidence indicates that the efficacy of many parameterization schemes varies significantly across seasons (Choi et al., 2017; Giorgi & Marinucci, 1991). For instance, in the western Himalayas, where distinct weather systems prevail in winter and summer, the impacts of microphysical and cumulus parameterization schemes on simulations exhibit marked seasonal differences (Dixit et al., 2023). Given that the impacts of other schemes vary seasonally, the impact of the STOFD scheme may also exhibit clear seasonal variations, warranting the systematic investigation. Furthermore, research based on a single season is inadequate to meet the demand of stable year-round simulation and prediction accuracy for meteorological services, such as the low-altitude economic meteorological services (WMO, 2015).

In parallel, given the complex topography and marked regional climate diversity across China, the influence of the STOFD scheme on the model simulations is therefore likely to vary substantially across regions and seasons (Wu et al., 2018). Systematic investigation into the seasonal applicability of STOFD in different characteristic regions of China is therefore urgently needed.

This paper systematically compares the influence of the STOFD scheme on the performance of Regional Climate Model Version 4 (RegCM4) in simulating the 10 m wind and precipitation over China in different seasons and reveals its seasonal dependence characteristics in different regions of China and the underlying physical mechanisms. The aim of this paper including: (a) quantify the impact of the STOFD scheme on the simulations of 10 m wind and associated precipitation responses in different seasons; (b) evaluate the seasonal applicability of the STOFD scheme in different characteristic regions of China; (c) reveal the mechanisms related to the seasonal differences in the impact of the STOFD scheme on the 10 m wind and precipitation simulations. Findings of this study may provide a foundation for refining the STOFD parameterization scheme and improving the accuracy of simulation and prediction. The rest of the paper is structured as follows: Section 2 describes the data, model, experimental design, and methodology. Section 3 presents a quantitative analysis of the seasonal differences in the effects of the STOFD scheme on the simulations of 10 m winds and precipitation. The associated physical mechanisms in different seasons are explored in Section 4. Finally, Section 5 provides the conclusion and discussion.

2. Data, Model, Experimental Design, and Methodology

2.1. Data

The data for model input are summarized as follows:

1. The 6-hourly ERA-Interim Reanalysis data set with the horizontal resolution of 1.5° × 1.5° (Dee et al., 2011) is used to provide atmospheric initial and lateral boundary conditions.
2. The weekly Optimum Interpolation Sea Surface Temperature (OISST) data with the horizontal resolution of 1° × 1° (Reynolds et al., 2002) is employed as the oceanic boundary condition.
3. The monthly European Space Agency Climate Change Initiative Essential Climate Variable (ESA CCI ECV) surface soil moisture combined product with the horizontal resolution of 0.25° × 0.25° (Dorigo et al., 2021) is used to initialize the land surface model.
4. The 30″ × 30″ (~1 × ~1 km) Global Multi-resolution Terrain Elevation Data (GMTED, Danielson & Gesch, 2011) is applied for the computation of the standard deviation (SD) of filtered sub-grid terrain elevation. This data set also provides the grid-scale elevation.

The data for model evaluation are summarized as follows:

1. The daily Asian Precipitation-Highly-Resolved Observational Data Integration Toward Evaluation (APHRODITE) grid precipitation with the horizontal resolution of 0.25° × 0.25° (Yatagai et al., 2012) from December 2010 to November 2015 is employed for assessing the accuracy of precipitation simulation.
2. The hourly ERA5 reanalysis data set with the horizontal resolution of 0.25° × 0.25° (ECMWF, 2020) during December 2010 to November 2015 is used to provide the 10 m wind data for evaluating near-surface wind simulations.

2.2. The RegCM4 Model and STOFD Scheme

The RegCM4, developed by the Abdus Salam International Center for Theoretical Physics (ICTP), stands as a pioneering regional climate model designed for climate downscaling (Dickinson et al., 1989; Gao & Giorgi, 2017). It has been widely adopted in East Asia for regional climate studies due to the demonstrated reliability in performance (Jo et al., 2024; Liu et al., 1994; Lu et al., 2019).

Among various STOFD parameterization schemes, the scheme developed by Beljaars et al. (2004, B04) performed better in enhancing simulation performance (Wang et al., 2020; Xue et al., 2021; X. Zhou et al., 2018, 2019). Therefore, this study employs the B04 scheme to investigate the seasonal differences in the influence of STOFD on the 10 m wind and precipitation simulations. The B04 scheme, initially implemented in RegCM4 by Gu et al. (2023a), has subsequently been employed in two dedicated studies to investigate the effects of the STOFD scheme on simulated precipitation over China in summer (Gu et al., 2023a; Y. Zhou et al., 2024). The STOFD at each model level is computed as:

$$\frac{\partial}{\partial z}\left(\frac{\tau_0}{\rho}\right) = -1.08372058 \times 10^{-7} \cdot \left|\vec{V}\right| \cdot \vec{V} \cdot e^{-\left(\frac{z}{1500}\right)^{1.5}} \cdot \sigma_{flt}^2 \cdot z^{-1.2} \quad (1)$$

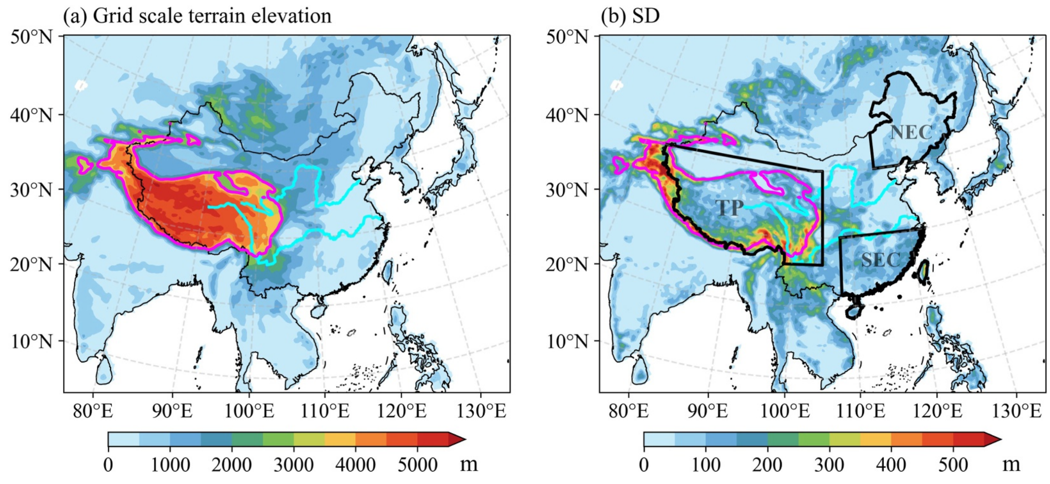

Figure 1. Spatial distribution of grid scale terrain elevation (a) and the standard deviation of filtered sub-grid terrain elevation (b) within the model domain. The thick black curves in each subplot outline the three primary sub-regions within China: the Southeastern China, Tibetan Plateau, and Northeastern China. The purple contours in each subplot indicate the 3,000 m elevation level (roughly equivalent to 700 hPa under standard conditions). The cyan curves in each subplot indicate the Yangtze River and Yellow River.

where z and ρ represent the height of the corresponding level above ground (unit: m) and air density (unit: $\mathrm{kg{\cdot}m^{-3}}$). τ_0 is wind stress (unit: $\mathrm{N{\cdot}m^{-2}}$) at each model grid, and $\vec{V}$ is the horizontal wind vector (unit: $\mathrm{m{\cdot}s^{-1}}$). σ_{flt} is the SD of filtered sub-grid terrain elevation (unit: m) computed following Beljaars et al. (2004). To ensure spectral reliability and minimize noise in the computed SD, the filter edges are set at $k = 0.00014\ \mathrm{m}^{-1}$ and $k = 0.0012\ \mathrm{m}^{-11}$, which correspond to spatial scales of 3–22 km. Details of the filtering procedure are provided in Beljaars et al. (2004, Appendix A). The parameter σ_{flt} is employed to extrapolate small-scale terrain spectra through the piecewise linear fit, serving as part of the spectral parameter in Equation 1. To calculate the STOFD, the lower limit of the integration wavenumber is set as $k_0 = 0.000628\ \mathrm{m}^{-1}$, corresponding to a half-wavelength of 5 km. This effectively restricts the topographic drag calculation to scales smaller than 5 km. Although the orographic filtering used in the STOFD scheme follows the methodology of previous studies, the choice of the filtering range may introduce some uncertainty into the representation of the unresolved small-scale terrain spectrum. Consequently, the separation between microscale and mesoscale topographic information may not be complete. Future work using higher-resolution topographic data sets and improved terrain-spectrum estimation methods could provide a more physically consistent and robust scale separation. This scheme applies a drag opposing the wind direction at each level, which is determined by wind speed, micro-scale terrain complexity, and height above ground of the corresponding level.

2.3. Experimental Design and Methodology

2.3.1. Experimental Design

To explore the influence of STOFD across seasons, two continuous simulations are conducted with the STOFD scheme activated (sensitivity experiment, SEXP) and deactivated (control experiment, CTRL) in RegCM4 from 1 June 2010 to 30 November 2015 with the initial six months as spin-up.

Both experiments employ a hydrostatic dynamic core with a 30-s time step and 3-hr output interval, featuring a horizontal resolution of 25 km and 23 vertical layers extending up to 50 hPa. The model domain (Figure 1), centered at (34°N, 107°E), comprises 320 × 240 grid points in the zonal and meridional directions, respectively. The model calculates long-wave radiation absorption-emission of cloud and gas particles, convection, land surface process, and solar radiation every hour, 30 s, 10 min, and 10 min, respectively.

Both experiments adopt the physical parameterization schemes as follows: the Tiedtke scheme (Tiedtke, 1996) over land and the Kain-Fritsch scheme (Kain & Fritsch, 1990) over the ocean for cumulus parameterization, the Zeng ocean flux scheme (Zeng et al., 1998), the sub-grid explicit moisture scheme (SUBEX, Pal et al., 2000), the

Holtslag planetary boundary layer scheme (Holtslag et al., 1990), the Community Land Model version 4.5 (CLM4.5, Oleson et al., 2010), and the radiation transfer module of the Community Climate Model version 3 (CCM3, Kiehl et al., 1998). The only difference in the model configuration between the SEXP and CTRL experiments is the adoption of the STOFD scheme or not. Both experiments output the 3-hr simulation results, and the model results from 1 December 2010 to 30 November 2015 are used for analysis.

2.3.2. Methodology

Model performances are evaluated using the root mean square error (RMSE) and Taylor score (TS, Taylor, 2001). The equations to calculate these metrics are shown below:

$$\text{RMSE} = \sqrt{\frac{1}{n}\sum_{i=1}^{n}(S_i - O_i)^2} \tag{2}$$

$$TS = \frac{4(1+R)}{\left(\sigma_{\text{norm}} + \frac{1}{\sigma_{\text{norm}}}\right)^2(1+R_0)} \tag{3}$$

$$R = \frac{\sum_{i=1}^{n}(S_i - \overline{S})(O_i - \overline{O})}{\sqrt{\sum_{i=1}^{n}(S_i - \overline{S})^2}\sqrt{\sum_{i=1}^{n}(O_i - \overline{O})^2}} \tag{4}$$

where S_i and O_i denote the simulated and observed (or reanalyzed) data at sample i, with n representing the total number of samples. The mean values of the simulated and observed (or reanalyzed) data over n samples are represented by $\overline{S}$ and $\overline{O}$, respectively. The correlation coefficient R between simulations and observations (or reanalysis) is calculated by Equation 4, and σ_{norm} represents the normalized SD of the simulation results ($\frac{\sigma_S}{\sigma_O}$, where σ_S and σ_O respectively represent the simulated SD and the observed SD). R_0 represents the attainable maximum correlation coefficient, which is set to 1 in this study. All significance tests are based on the Student's t-test (Student, 1908).

To visually demonstrate the water vapor differences induced by the STOFD scheme, the vertically integrated water vapor flux convergence from the surface to 300 hPa is calculated as:

$$C = -\frac{1}{g}\int_{p_s}^{300\text{hPa}} \nabla \cdot (qV)\, dp \tag{5}$$

where C is the vertically integrated water vapor flux convergence (units: kg·m^{-2}·s^{-1}), g is the gravitational acceleration (approximately 9.8 m·s^{-2}), p_s is the surface pressure (Pa), q is specific humidity (kg · kg^{-1}), V is the horizontal wind vector (m · s^{-1}), and $\nabla\cdot$ denotes the horizontal divergence operator. Positive values of C indicate net water vapor convergence, favoring precipitation.

Driven by regional differences in dominant weather systems and circulation configurations, the seasonal impacts of STOFD vary accordingly in different sub-regions. Based on a comprehensive analysis, three core representative sub-regions within China are selected to systematically investigate the seasonal influence of STOFD on regional climate and key physical processes across China, as shown in Figure 1: the Southeastern China (SEC), typically dominated by East Asian monsoon system; TP, characterized by complex micro-scale topography and dominated by mid-latitude westerlies; and the Northeastern China (NEC), located downstream of both the East Asian monsoon and mid-latitude westerlies. These selected sub-regions encompass distinct climatic backgrounds and contrasting topographic characteristics, thereby ensuring the broad representativeness of the research findings.

3. Results

3.1. Impact of STOFD Scheme on the Simulations of 10 m Wind

The CTRL experiment captures the overall spatial structure and seasonal variations of the 10 m wind field in the ERA5 reanalysis (Figure 2). In both the CTRL experiment and the ERA5 reanalysis, the TP is dominated by

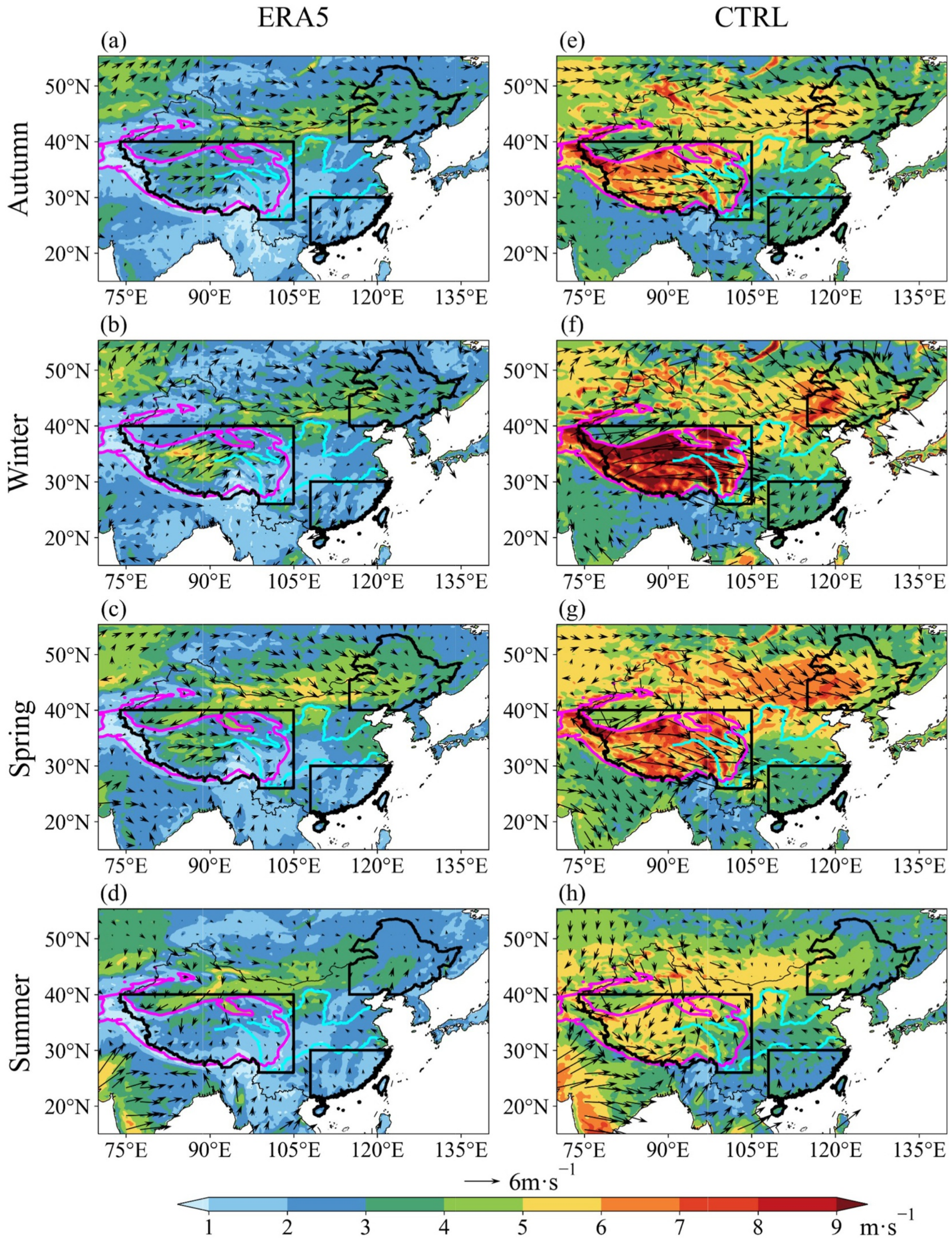

Figure 2. Spatial distribution of mean 10 m wind in each season from ERA5 reanalysis data (a–d) and CTRL experiment (e–h). The thick black curves in each subplot outline the three primary sub-regions within China. The purple contours (cyan curves) in each subplot indicate the 3,000 m elevation level (Yangtze River and Yellow River).

westerlies from autumn to spring (Figures 2a–2c and 2e–2g). In summer, a cyclonic circulation is induced by the thermal forcing over the TP (Figures 2d and 2h). Influenced by the East Asian summer monsoon, eastern China also exhibits markedly different wind directions in summer compared to the other seasons. In the NEC (SEC), the prevailing wind is westerly (northerly or erratic) from autumn to spring, shifting to southerly in summer (Figure 2).

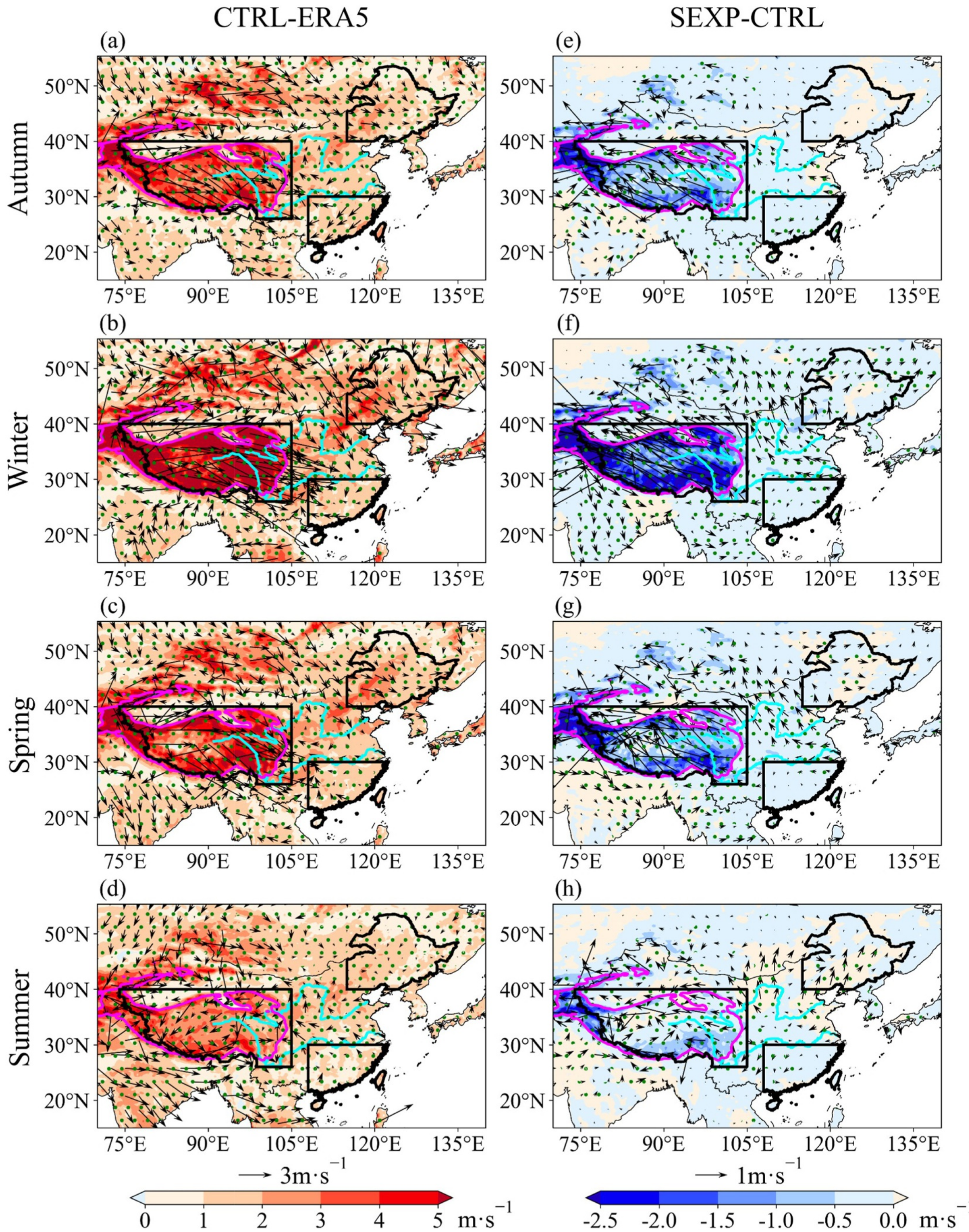

Figure 3. Spatial distribution of mean 10 m wind bias in each season in the CTRL experiment (a–d) and spatial distribution of the mean differences of the simulated 10 m winds in each season between the SEXP and CTRL experiments (e–h). The thick black curves in each subplot outline the three primary sub-regions within China. The purple contours (cyan curves) in each subplot indicate the 3,000 m elevation level (the Yangtze River and Yellow River). The green dots denote the differences significant at the 90% confidence level.

Compared to the ERA5 reanalysis, the simulated wind speeds in the CTRL experiment exhibit a consistent positive bias, particularly over the TP (Figures 3a–3d). Among all seasons, the most substantial overestimation occurs in winter, with the bias exceeding 5.0 m·s^{-1} over most parts of the TP, while summer shows the smallest bias.

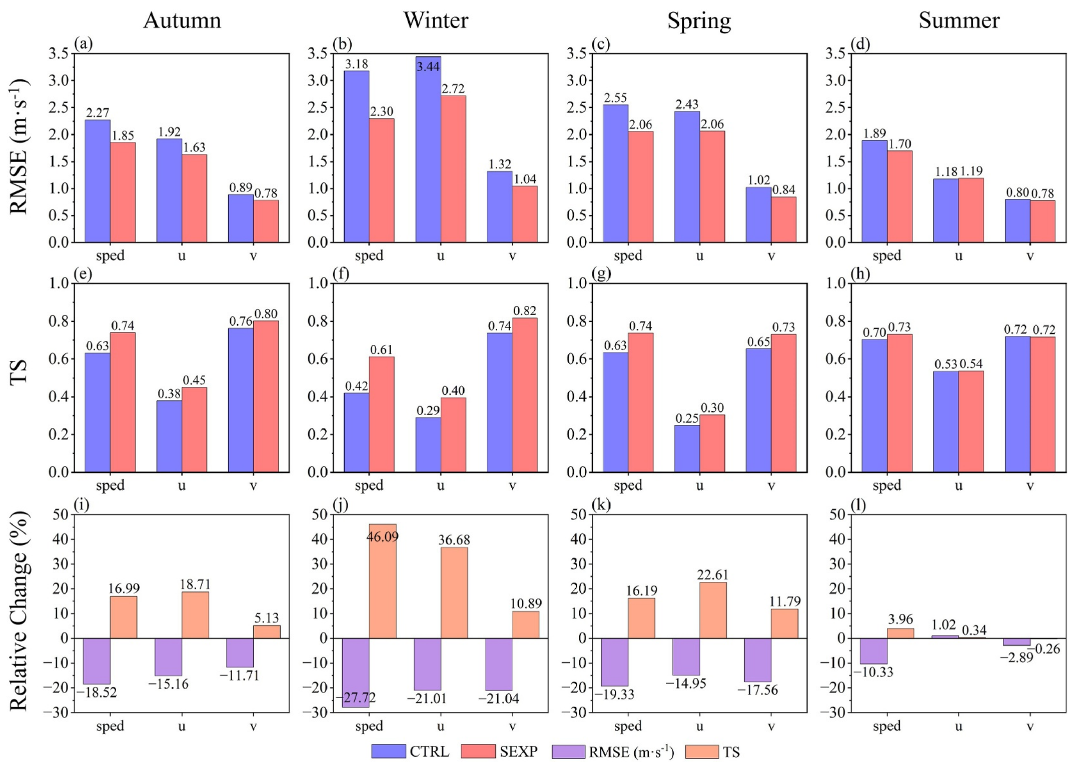

Figure 4. The root mean square error (RMSE) (a–d) and Taylor score (TS) (e–h) for the speed, *u* and *v* components of 10 m wind within China in each season simulated by the CTRL and SEXP experiments. The relative changes of RMSE and TS for the speed, *u* and *v* components of 10 m wind within China in each season in the SEXP experiment compared to the CTRL experiment, respectively (i–l), calculated by (SEXP-CTRL)/CTRL × 100%.

The impact of the STOFD scheme demonstrates distinct regional and seasonal characteristics in improving 10 m wind simulations across China. The STOFD scheme exerts marked enhancements in 10 m wind simulation performance, with the strongest weakening effect on 10 m winds in winter and the weakest in summer among all seasons (Figures 3e–3h). Even in summer, the season with the weakest effects of the STOFD scheme, the simulated 10 m wind speed reductions exceed 2.5 m·s^{-1} over the western TP. The most pronounced effect of the STOFD scheme on 10 m wind is concentrated over the TP and its surroundings (the Tianshan Mountains and Pamir Plateau) in all seasons, where the magnitude of improvement varies with the seasonal variations in the intensity of the circulation background (Figures 2e–2h and 3e–3h).

From autumn to spring, the STOFD scheme induces significant southeasterly wind differences in 10 m wind over TP, weakening the westerlies in the CTRL experiment (Figures 3e–3g). While in summer, there is no uniform direction for the difference in 10 m wind over TP between the SEXP and CTRL experiments (Figure 3h). In the SEC, the STOFD scheme yields modest but consistent improvements in 10 m wind across all seasons (Figures 3e–3h). By contrast, in the NEC, the STOFD scheme tends to increase 10 m wind speeds, introducing new errors. The errors induced by the STOFD scheme are minimal in winter and most substantial in summer in the NEC, accompanied by notable southerly wind differences in 10 m wind in summer. The STOFD-induced 10 m wind differences do not exhibit a simple inverse correspondence to the background wind field. The spatial mismatch is observed in NEC throughout the year, while over the TP it is particularly pronounced during summer.

Across China, the STOFD scheme significantly improves the simulated speed and *u* and *v* components of 10 m wind, with the wind speed exhibiting a greater relative improvement than either directional component (Figure 4). From Figures 4i–4l, the enhancement is the most pronounced in winter among all seasons, with the RMSE (TS) of 10 m wind speed simulation reduced by 27.72% (increased by 46.09%), while the least improvement is noticed in summer, with the RMSE (TS) of 10 m wind speed simulations reduced by 10.33% (increased by 3.96%).

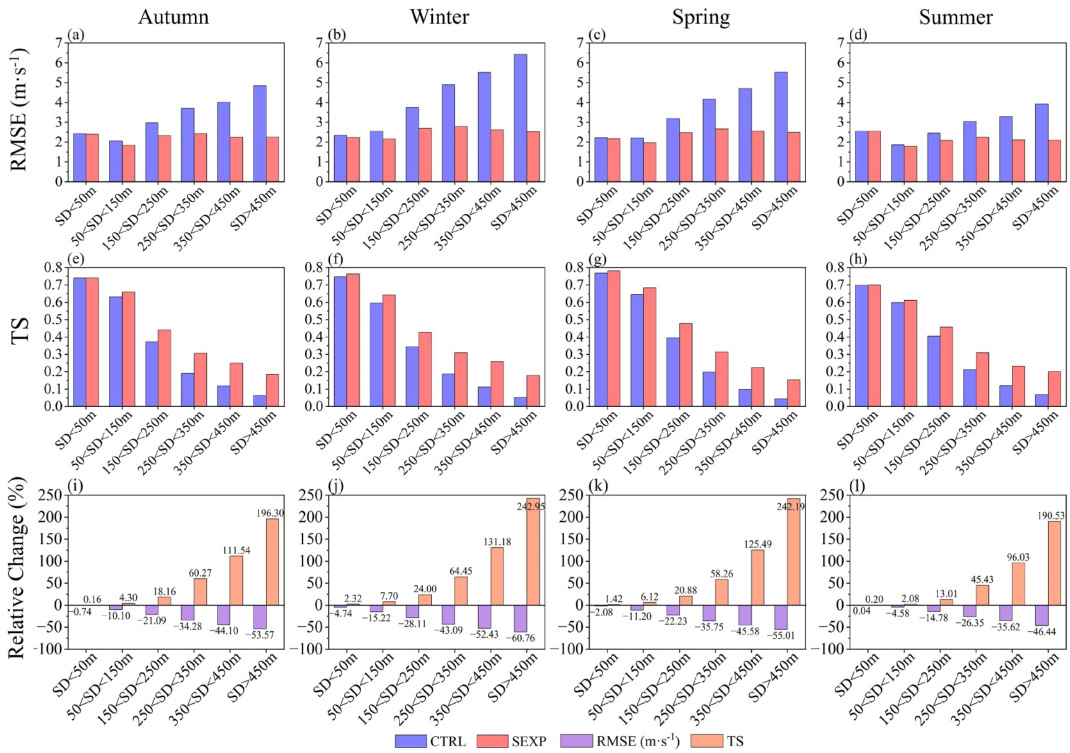

Figure 5. Root mean square error (RMSE) (a–d) and Taylor score (TS) (e–h) of 10 m wind speed at grids with different sub-grid terrain standard deviation across the model domain in each season simulated by the CTRL and SEXP experiments. The relative changes of RMSE and TS in the SEXP experiment compared to the CTRL experiment (i–l) are calculated by (SEXP-CTRL)/CTRL × 100%.

Higher sub-grid terrain SD indicates more complex micro-scale terrains. In the CTRL experiment, the RMSE (TS) of the simulated 10 m wind speed increases (decreases) with the increasing micro-scale terrain complexity in various seasons (Figures 5a–5h). In the SEXP experiment, the RMSE of the simulated 10 m wind speed remains nearly constant across different micro-scale terrain complexity, indicating that the introduction of the STOFD scheme has nearly eliminated the RMSE of simulated 10 m wind speed generated by the insufficient representation of micro-scale terrain in the model. Across almost all sub-grid terrain SD values, the STOFD scheme reduces RMSE and increases TS. The improvement in simulated 10 m wind accuracy across all seasons is positively correlated with micro-scale terrain complexity, with regions of more complex micro-scale terrain exhibiting greater enhancement (Figures 5i–5l). This indicates that inadequate representation of micro-scale terrain features is a major source of bias in the model simulations. The improvement induced by the STOFD scheme is particularly pronounced where the sub-grid terrain SD exceeds 450 m, achieving the reductions of RMSE by 46.44%–60.76% and enhancements of TS by 190.53%–242.95% during all seasons. Under all terrain conditions, the improvement of 10 m wind simulations shows clear seasonal differences. The STOFD scheme generates the most significant improvement in the 10 m wind speed simulations during winter and the lowest improvement in summer among all seasons.

The improvement of simulated winds induced by the STOFD is significant not only at the 10 m level but also within the near-surface portions of the circulation at different pressure levels (Figure 6). Figure 6i presents the distribution of the near-surface grids across different pressure levels. The definition of the near-surface portion: the grids lying within 1 km above the ground at the corresponding pressure level, is provided in Figure 6j. The most substantial reduction induced by the STOFD scheme in RMSE occurs at 500 hPa from autumn to spring (Figures 6a–6c), whereas in summer, the most pronounced improvement occurs at 600 hPa (Figure 6d). This finding further highlights the significant influence of the STOFD scheme generated by the complex micro-scale terrain in the TP on wind simulations. Consistent with the 10 m wind results, the impact of the STOFD scheme on near-surface circulation is the strongest in winter among all seasons, with a 41.06% decrease in RMSE at 500 hPa, and the weakest improvement in summer, with a 19.57% decrease at 600 hPa (Figures 6a–6d).

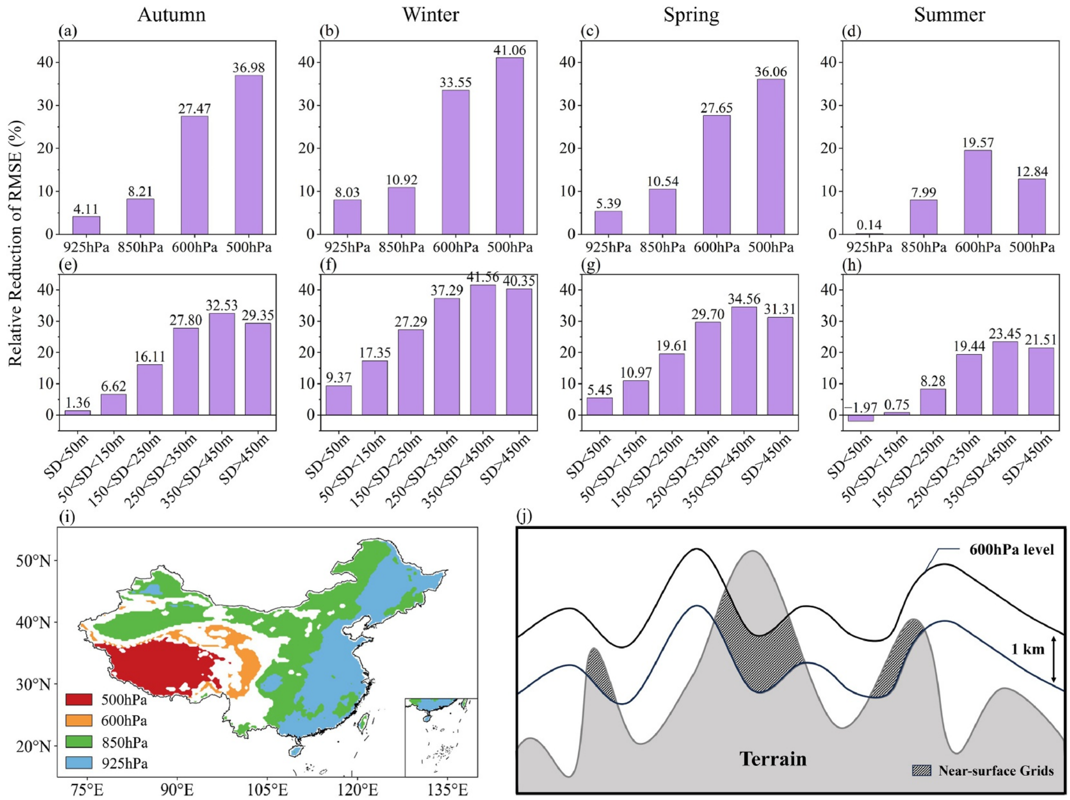

Figure 6. (a–d) Relative reduction of root mean square error (RMSE) induced by the sub-grid turbulent orographic form drag (STOFD) scheme in the simulated near-surface wind speed within China at 925, 850, 600, and 500 hPa in each season (calculated only for the grids lying within 1 km above the ground at the corresponding pressure level, as shown in panels (i and j), calculated by (CTRL-SEXP)/CTRL × 100%. (e–h) Relative reduction of RMSE induced by the STOFD scheme in the simulated near-surface wind speed at grids with different sub-grid terrain standard deviation across China in each season. (i) Distribution of the near-surface grids involved in the calculation across different pressure levels. (j) Schematic diagram of the near-surface grids involved in the calculation lying within 1 km above the ground at the corresponding pressure level (Take 600 hPa as an example).

The simulation improvement induced by the STOFD for near-surface wind speeds over the regions with different sub-grid terrain SD values shows a pattern similar to that for the 10 m wind, where the improvement increases with sub-grid terrain SD (Figures 6e–6h). However, the most significant improvement shifts from sub-grid terrain SD values exceeding 450 m to the range of 350–450 m, achieving the most significant reductions of RMSE by 41.56% in winter and the least significant reductions of RMSE by 23.45% in summer among all seasons.

The near-surface circulation simulation improvement assessment aligns with the 10 m wind analysis, confirming the reliability of both. The decrease in the improvement capability of the STOFD scheme in the circulation indicates that the STOFD effect weakens as the distance from the ground increases.

Overall, the effect of STOFD exhibits pronounced seasonal variability and distinct topographic dependency in improving 10 m wind and circulation simulations across China. The simulation improvements induced by the STOFD scheme are the strongest in winter and the weakest in summer among all seasons, and show a consistently positive relationship with micro-scale terrain complexity.

3.2. Impact of STOFD Scheme on the Simulations of Precipitation

Beyond the direct impact on wind, the STOFD scheme also significantly modulates precipitation through the influence on water vapor transport and associated atmospheric processes. The involvement of multiple, interacting processes and high sensitivity to circulation configuration in precipitation simulations necessitates regional analysis of simulation results.

10.1029/2025JD046293

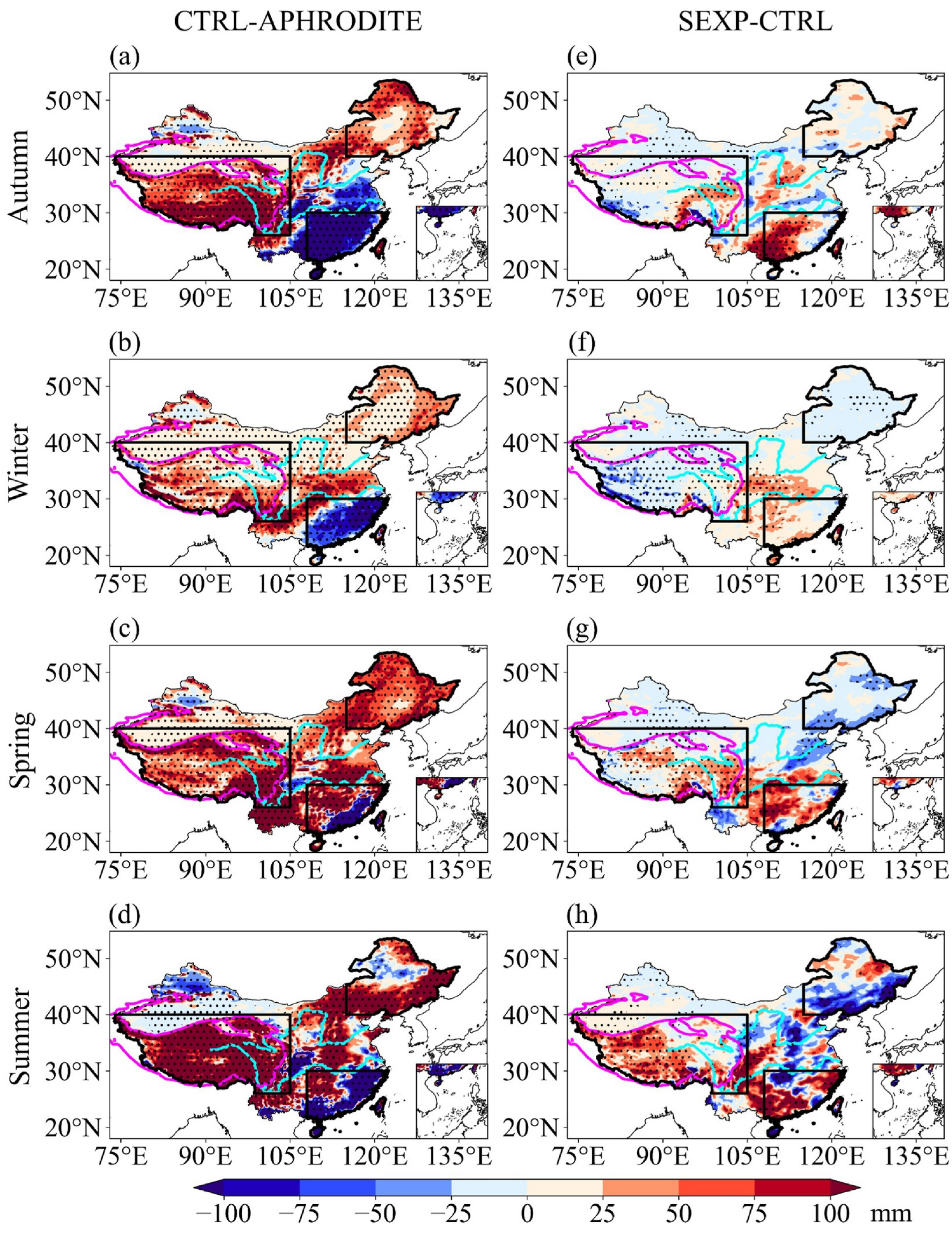

Figure 7. The spatial distribution of precipitation simulation bias within China in each season in the CTRL experiment (a–d). The spatial distribution of simulated precipitation differences within China in each season between the SEXP and CTRL experiments (e–h). The thick black curves in each subplot outline the three primary sub-regions within China. The purple contours (cyan curves) in each subplot indicate the 3,000 m elevation level (the Yangtze River and Yellow River). The black dots in each subplot denote differences significant at the 90% confidence level.

During winter, spring, and summer, the distribution of simulated precipitation in the CTRL experiment exhibits a positive bias in the northwest part and a negative bias in the southeast part of the SEC (Figures 7b–7d). While the CTRL experiment underestimates the autumn precipitation in almost the entire SEC (Figure 7a). The adoption of the STOFD scheme slightly increases the simulated precipitation in winter, and markedly increases simulated precipitation in spring relative to the CTRL experiment, correcting the negative bias in the southeast part but

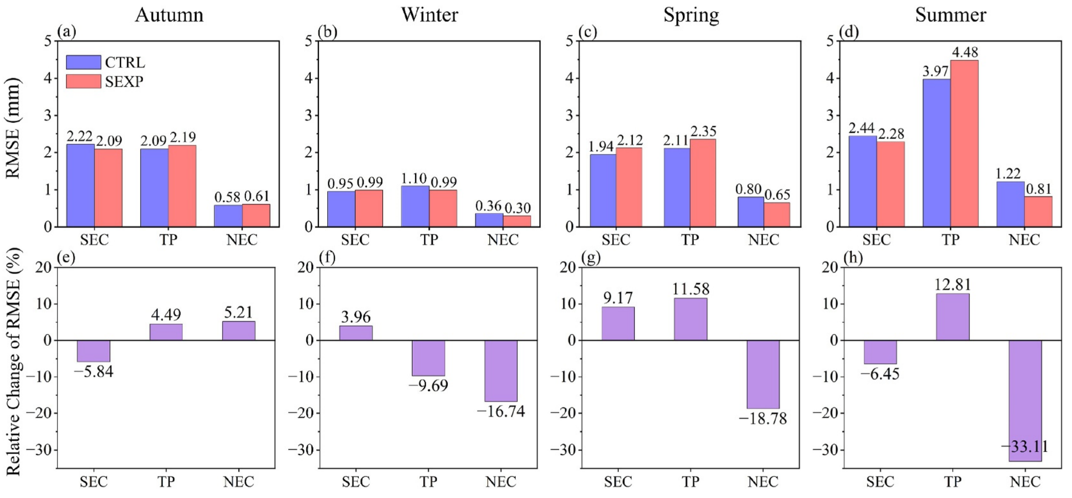

Figure 8. The root mean square error (RMSE) of the simulated precipitation over the three sub-regions in each season (a–d). The relative changes of RMSE in the SEXP experiment compared to the CTRL experiment (e–h) are calculated by (SEXP-CTRL)/CTRL × 100%.

intensifying the positive bias in the northwest part of the SEC (Figures 7f and 7g). The adoption of the STOFD scheme improves the precipitation simulation across both the positive and negative biases in summer (Figure 7h). During autumn, the STOFD scheme leads to a substantial increase in the simulated precipitation, significantly reducing the negative bias of simulated precipitation (Figure 7a). The CTRL experiment tends to overestimate precipitation over the TP across all seasons (Figures 7e–7h). The STOFD scheme can partially reduce the overestimation of simulated precipitation over the western TP but tends to increase the bias over the eastern TP from autumn to spring (Figures 7e–7g). However, the STOFD scheme exhibits the opposite effect in summer relative to other seasons, further increasing the precipitation simulation deviation over the TP (Figure 7h). The precipitation over the NEC simulated by the CTRL experiment shows widespread positive biases across seasons, except for isolated negative biases during summer (Figures 7a–7d). The STOFD scheme effectively mitigates these deviations of simulated precipitation, reducing the positive biases in all seasons except autumn and increasing precipitation in the regions with negative biases in summer (Figures 7e–7h).

To quantitatively evaluate the seasonal differences in the impact of the STOFD scheme on the precipitation simulation, the RMSE of the simulated precipitation over the three sub-regions is calculated, deriving the corresponding relative improvements induced by the STOFD scheme (Figure 8).

In the SEC, the STOFD scheme reduces the RMSE of simulated precipitation by 0.13 and 0.16 mm in autumn and summer (Figures 8a and 8d), with relative improvements of 5.84% and 6.45% (Figures 8e and 8h), respectively, while showing limited improvement in winter and spring. The most notable improvement of precipitation simulation over the TP induced by the STOFD scheme is noticed in winter among all seasons, with the RMSE reduction of 0.11 mm, representing a 9.69% relative improvement (Figures 8b and 8f). However, the improvement of simulated precipitation over the TP induced by the STOFD scheme in other seasons remains limited. Adopting the STOFD scheme substantially reduces the RMSE of precipitation simulation in the NEC from winter to summer, except in autumn. The most significant improvement in the NEC is observed in summer, with the RMSE reduction of 0.41, equating to a 33.11% relative improvement compared to the CTRL experiment (Figures 8d and 8h).

Overall, the impact of the STOFD scheme on precipitation simulations exhibits even more pronounced seasonal differences than that on the wind simulations. The STOFD scheme significantly reduces the positive precipitation simulation bias over the TP in winter, while enhancing the simulation performance over the SEC during summer and autumn. The STOFD scheme can clearly reduce the positive precipitation simulation bias in the NEC across all seasons, with the most significant correction in summer.

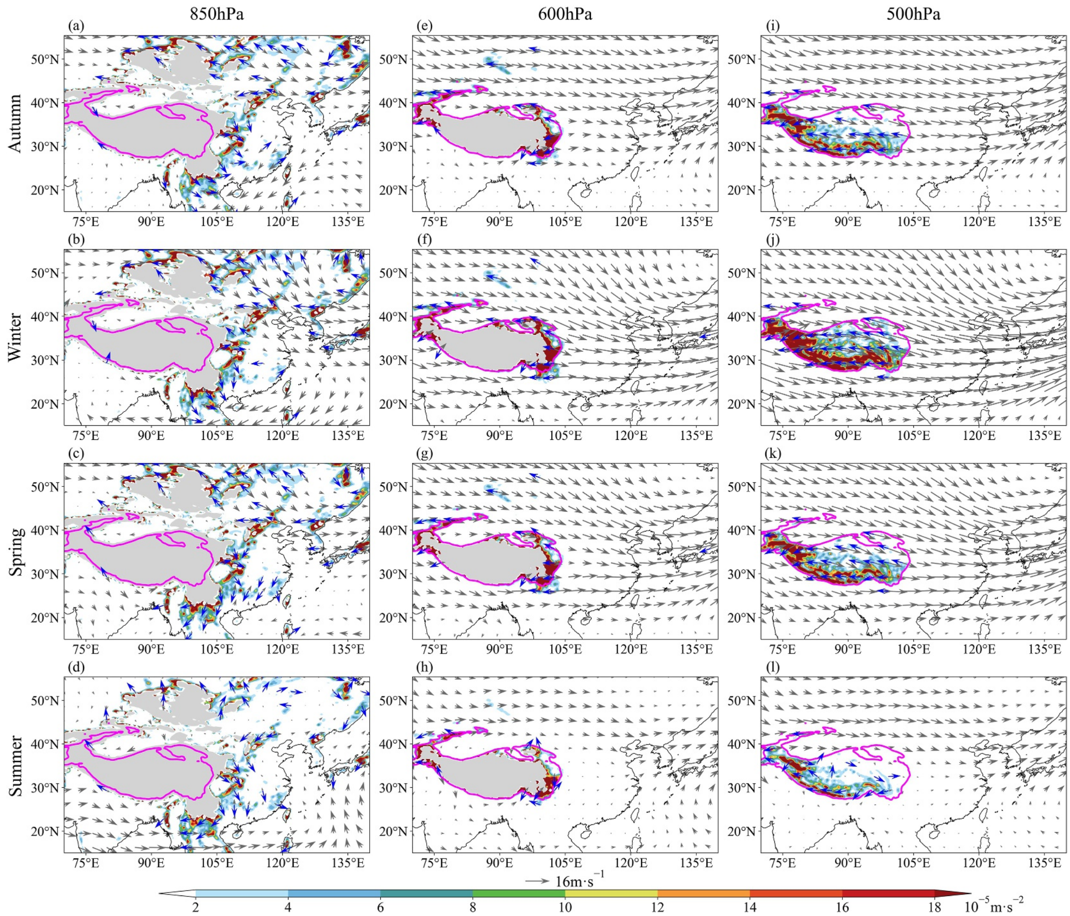

Figure 9. The wind vectors simulated by the CTRL experiment (gray vectors) and the directions (blue vectors, plotted only for magnitudes $>10^{-5}$ m·s^{-2}) and magnitudes (color shadings) of sub-grid turbulent orographic form drag in the SEXP experiment at 850 hPa (a–d), 600 hPa (e–h), and 500 hPa (i–l) in each season. The Gray shadings in each subplot indicate the terrain elevation above the corresponding pressure level. The purple contours in each subplot indicate the 3,000 m elevation level.

4. Possible Mechanisms

To elucidate the mechanisms by which the STOFD scheme influences the simulations of 10 m wind and precipitation, the spatial distribution of background circulation at multiple levels in the CTRL experiment, along with the corresponding STOFD magnitude and vector direction, is illustrated in Figure 9. As derived from Equation 1, the direction of STOFD is determined by wind direction, while its magnitude depends on the sub-grid terrain SD, wind speed, and the height above the ground. Therefore, the direction of STOFD consistently opposes the background wind, with the dominant influence concentrated over the TP and its surroundings within the 600-500 hPa levels that correspond to the near-surface layer characterized by the most complex topography on the plateau, with a characteristic magnitude achieving 10^{-4} m·s^{-2} (Figures 9e–9l).

While the sub-grid terrain SD remains constant and the height above ground varies minimally across seasons, wind speed and direction exhibit marked seasonal variability. Consequently, the STOFD displays significant seasonal differences in both magnitude and direction. Overall, with wind intensity in the CTRL experiment peaking in winter and reaching a minimum in summer across all seasons over China (Figures 2e–2h), the STOFD follows the same seasonal cycle (Figure 9). As a result, the weakening of 10 m wind induced by the STOFD scheme is the strongest (weakest) in winter (summer) among all seasons.

Driven by seasonal migration of the subsolar point, the meridional migration and intensity modulation of the westerlies in the CTRL experiment produce distinct circulation regimes in different seasons. The westerlies reach the maximum intensity and southernmost position during winter, while weakening and shifting northward in summer. The westerlies prevail over the TP and its surroundings from autumn to spring (Figures 9e–9g and 9i–9k). While in summer, the combined influence of the northward-displaced westerlies and the thermally induced cyclonic circulation over the TP confines the primary westerlies in the CTRL experiment to the further north, including the north of TP, Tianshan Mountains, and Pamir Plateau (Figures 9h and 9l). Correspondingly, the STOFD exhibits strong seasonality. Its magnitude peaks in winter, and the most pronounced STOFD is above the TP and its surroundings, maintaining a consistent westward orientation from autumn to spring (Figures 9e–9g and 9i–9k). During summer, when the STOFD intensity minimizes, the dominant drag vectors adopt more varied directions, maintaining westward only along the south sides of the TP, the Pamir Plateau, and the Tianshan Mountains (Figures 9h and 9l). From autumn to spring, the STOFD distribution over TP aligns with the 10 m wind speed differences between the SEXP and CTRL experiments, indicating a direct influence of STOFD on the 10 m wind simulation over this region in the SEXP experiment. However, the STOFD distribution in summer partly deviates from the 10 m wind speed differences between the SEXP and CTRL experiments, implying that indirect effects also contribute to the 10 m wind simulation in the SEXP experiments.

Furthermore, modulated by the seasonal differences of the East Asian monsoon within the background circulation, the STOFD direction in the SEC and NEC exhibits pronounced seasonality (Figures 9a–9d). In all seasons, the STOFD at 850 hPa in the SEC aligns with the 10 m wind differences between the SEXP and CTRL experiments. In contrast, the wind differences in the NEC between the SEXP and CTRL experiments deviate markedly from the local STOFD at 850 hPa. Consequently, the STOFD acts to directly weaken the 10 m wind simulation in the SEXP experiment over the SEC, while the 10 m wind differences in the NEC between the SEXP and CTRL experiments may be influenced by a downstream effect arising from the STOFD-induced weakening of the westerlies and the East Asian monsoon.

Given the maximum magnitude of STOFD over the TP and its surroundings, the main impact of the STOFD scheme on the circulation manifests through the deceleration of westerlies above the region (Figures 10e–10l). According to the quasi-geostrophic approximation of the zonal momentum equation considering STOFD (R. Li et al., 2023):

$$\frac{du}{dt} - fv = -\frac{1}{\rho}\frac{\partial p}{\partial x} + \text{STOFD}_x \tag{6}$$

Here, f is the Coriolis parameter, STOFD_x is zonal component of the STOFD. For large-scale stable flows with little downstream variation, the equation satisfies both the stationary and non-advection conditions ($\frac{du}{dt} = 0$). Under this condition, the zonal momentum equation reduces to a generalized geostrophic balance, expressed as:

$$-fv_a = \text{STOFD}_x \tag{7}$$

As indicated by Equation 7, STOFD over the TP and its surroundings not only decelerates westerlies but also induces an ageostrophic southerly component (v_a), resulting in southeasterly wind differences between the SEXP and CTRL experiments (Figures 10e–10l). Affected by the southerly component of the southeasterly wind differences between the SEXP and CTRL experiments, a horizontal divergence difference ($\frac{\partial v}{\partial y} > 0$) at 500 hPa occurs on the south side of the southeasterly wind difference, while a horizontal convergence difference ($\frac{\partial v}{\partial y} < 0$) at 500 hPa occurs on the north side. In accordance with meridional mass continuity $\frac{\partial v}{\partial y} + \frac{\partial \omega}{\partial p} = 0$, therefore vertical convergence (divergence) difference satisfying $\frac{\partial \omega}{\partial p} < 0$ ($\frac{\partial \omega}{\partial p} > 0$) at 500 hPa occurs on the south (north) side of the southeasterly wind differences, leading to ascending (descending) motion difference between the SEXP and CTRL experiments. Then, there is a meridional circulation difference across the southeasterly wind differences between the SEXP and CTRL experiments (Figure 11). On the south side of the southeasterly wind differences, the ascending motion difference induces a vertical divergence difference satisfying $\frac{\partial \omega}{\partial p} > 0$ at low levels. According to the zonal continuity equation $\frac{\partial u}{\partial x} + \frac{\partial \omega}{\partial p} = 0$, the vertical divergence difference implies $\frac{\partial u}{\partial x} < 0$, indicating horizontal airflow convergence difference forms a cyclone difference (Figure 10). Conversely, the north side of the southeasterly wind differences experiences a vertical convergence difference due to descending ascending motion difference ($\frac{\partial \omega}{\partial p} < 0$) between the SEXP and CTRL experiments, which yields horizontal airflow divergence forms an anticyclone difference ($\frac{\partial u}{\partial x} > 0$). The formation of cyclone and

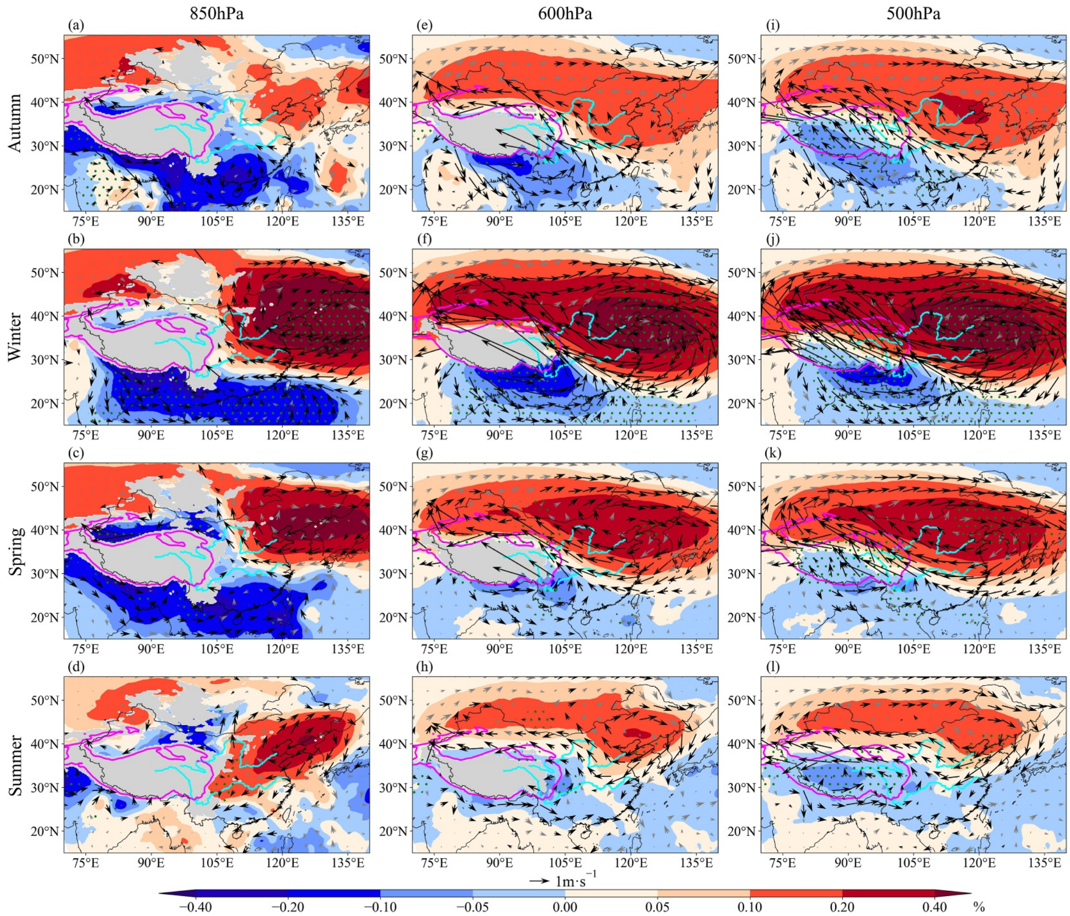

Figure 10. Differences in wind (vectors) and the relative differences of geopotential height ((SEXP-CTRL)/CTRL × 100%), color shadings) at 850 hPa (a–d), 600 hPa (e–h), and 500 hPa (i–l) between the SEXP and CTRL experiments in each season. The Gray shadings in each subplot indicate the terrain elevation above the corresponding pressure level. The purple contours (cyan curves) in each subplot indicate the 3,000 m elevation level (the Yangtze River and Yellow River). The green dots in each subplot denote the relative differences between the SEXP and CTRL experiments in geopotential height significant at the 90% confidence level. The vectors in black in each subplot indicate the differences in wind between the SEXP and CTRL experiments over the 90% significance level.

anticyclone differences promotes the westerly wind differences on both sides of the southeasterly wind differences. The differences in simulated atmospheric circulation between the SEXP and CTRL experiments are attributable not only to the mechanisms discussed above but also to various nonlinear feedback.

The secondary meridional circulation difference between the SEXP and CTRL experiments induced by the STOFD scheme shifts seasonally in concert with the westerlies in the CTRL experiment (Figure 11). The shear line between ascending and descending differences is situated near 36°N in winter, migrates northward to approximately 38°N during spring and autumn, and advances further north to around 42°N in summer.

Therefore, the horizontal circulation differences between the SEXP and CTRL experiments shift meridionally in response to the displacement of the westerlies in the CTRL experiment. In the SEXP experiment, the dynamical response of STOFD remains consistent from autumn to spring, but exhibits pronounced seasonal variations in location and intensity, which are attributed to seasonal meridional displacement and intensity variations of the background circulation. In winter, the westerlies in the CTRL experiment reach the greatest intensity and southernmost extent. Therefore, the STOFD-induced southeasterly wind differences between the SEXP and CTRL experiments correspondingly occur with the largest magnitude at the lowest latitudes among all seasons (Figures 10b, 10f, and 10j). During spring and autumn, the westerlies in the CTRL experiment are displaced northward and weaken relative to winter, and the associated southeasterly wind differences between the SEXP

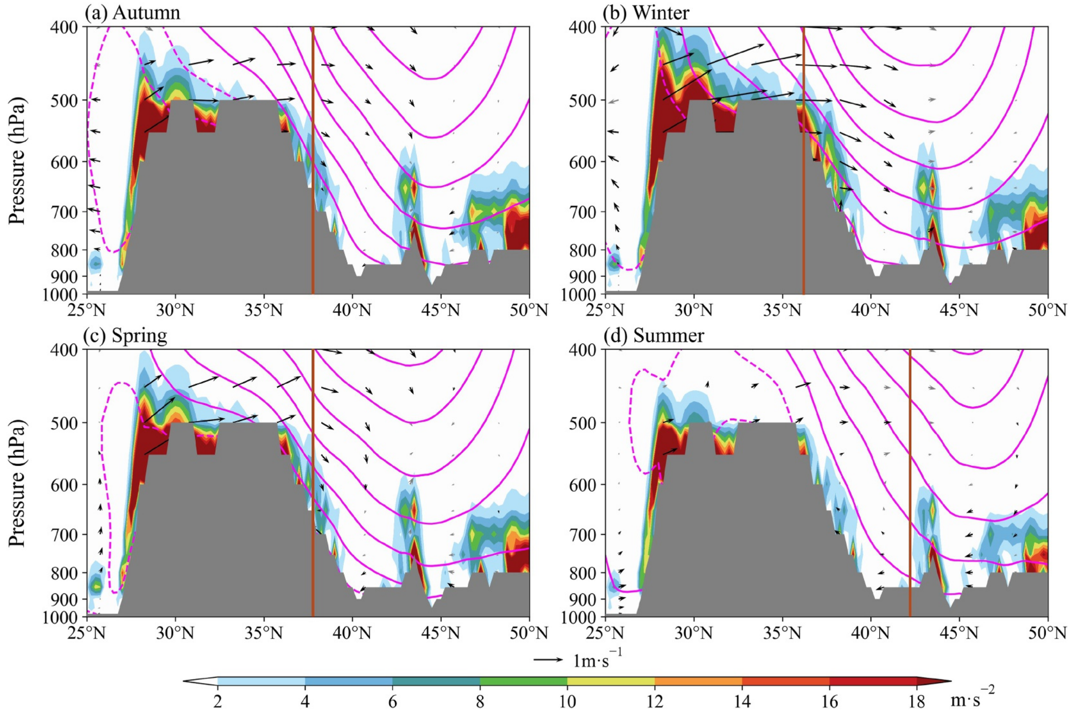

Figure 11. Pressure-latitude cross section of atmospheric circulation differences (vectors; black vectors indicate differences significant at the 90% confidence level, vertical velocity enlarged by 100 times), geopotential height differences between the SEXP and CTRL experiments (purple contours; unit: gpm, at an interval of 2 gpm), and sub-grid turbulent orographic form drag (color shadings) regionally averaged along 85°–95°E in each season. The brown lines represent the shear line between the ascending and descending air flows. The gray shadings indicate terrain.

and CTRL experiments likewise appear at relatively higher latitudes with reduced magnitude compared to winter (Figures 10a, 10c, 10e, 10g, 10i, and 10k). By contrast, the westerlies in summer locates the northernmost with the weakest strength among all seasons, where only the Pamir Plateau and the Tianshan Mountains induce STOFD that have significant effects (Figures 10d, 10h, and 10l). Therefore, the resulting southeasterly wind differences are the weakest among all seasons and remain restricted to the northern TP, contrasting with the entire plateau southeasterly wind differences observed in other seasons, with substantially reduced spatial coverage. The vertical motion differences between the SEXP and CTRL experiments flanking these southeasterly wind differences persist but shift northward relative to other seasons (Figure 11d). This configuration, combined with low-pressure differences over the southern plateau, reinforces the cyclonic circulation above the TP in the CTRL experiment, establishing a summer circulation regime markedly different from other seasons (Figure 10). The reinforced cyclonic circulation in the SEXP experiment explains why the improvement of the near-surface circulation at 500 hPa generated by STOFD during summer is weaker than that at 600 hPa level.

Although the STOFD primarily originates over the TP and its surroundings, the resulting southeasterly wind differences between the SEXP and CTRL experiments are not confined to the TP and its surroundings but continue to propagate downstream, establishing a low-pressure difference and cyclonic difference over the SEC at 850 hPa, and a high-pressure difference and anticyclonic difference over the NEC at 850 hPa, respectively (Figures 10a–10d). The 850 hPa circulation differences over the SEC between the SEXP and CTRL experiments do not correspond to the local STOFD but instead mirror mid-level circulation differences. Thus, they arise mainly from the indirect mechanism of mid-level STOFD hindering the westerlies. Due to the domination of downstream effects from the westerly wind differences between the SEXP and CTRL experiments, this indirect process obscures STOFD's direct impact on the East Asian monsoon. Given this, the downstream effects of the monsoon affected by STOFD on circulation over the NEC are minimal. The circulation differences in the NEC between the SEXP and CTRL experiments are primarily attributable to the indirect impacts of the deceleration of westerlies induced by the STOFD.

The position and structure of these downstream circulation differences in the SEXP experiment compared to the CTRL experiment also vary seasonally. In winter, the cyclonic difference remains over the southern part of SEC, exerting limited influence on local precipitation (Figure 10b). During autumn and spring, the difference shifts northward, positioning the cyclonic differences directly over the SEC and creating favorable dynamic conditions for precipitation (Figures 10a and 10c). During summer, the relatively weak circulation differences induced by the STOFD consequently lead to the least pronounced cyclonic differences over the SEC (Figure 10d). Although being the weakest, the modified summer circulation pattern in the SEXP experiment establishes a dynamic condition that aligns well with the bias of simulated precipitation.

Furthermore, the anticyclonic differences generated by the STOFD over the NEC migrate meridionally in phase with the seasonal displacement of the westerlies, establishing favorable dynamic conditions for precipitation reduction. These anticyclonic differences reach their southernmost position along the periphery of the NEC in winter and shift to the northernmost location among all seasons in the central NEC during summer (Figures 10a–10d). Although the STOFD intensity is the weakest in summer among all seasons, the associated 850 hPa anticyclonic differences over the NEC between the SEXP and CTRL experiments are more pronounced than those in autumn (Figures 10a and 10d). The location of 850 hPa anticyclonic differences in summer aligns closely with the area of positive precipitation simulation bias in the CTRL experiment (Figure 10d). Consequently, the anticyclonic differences between the SEXP and CTRL experiments during summer demonstrate a significant reduction in the simulated precipitation bias over the NEC.

Although the 10 m wind differences between the SEXP and CTRL experiments over the NEC induced by the STOFD show only a weak inverse correlation with the background 10 m wind in the CTRL experiment among all seasons, they exhibit consistency with the STOFD-induced wind differences at 850 hPa (Figures 10a–10d). This suggests that the 10 m wind response is not solely a direct result of the STOFD forcing, but is also modulated by circulation adjustments triggered by the scheme (Figure 10). The seasonal variations in background wind intensity in the CTRL experiment lead to the strongest winter and weakest summer improvement in 10 m wind simulations. The meridional movement of the westerlies in the CTRL experiment indirectly promotes significant differences in the spatial distribution of summer 10 m wind differences compared to other seasons.

These seasonally dependent dynamic processes constitute a key mechanism governing regional simulated 10 m wind and precipitation differences between the SEXP and CTRL experiments.

The distinct seasonal circulation differences between the SEXP and CTRL experiments that drive corresponding seasonal variations in water vapor transport differences (Figure 12). From autumn to spring, the TP is primarily influenced by southeasterly wind differences, which block water vapor transport, resulting in moisture divergence differences over the western TP between the SEXP and CTRL experiments (Figures 12a–12c). Throughout all seasons except summer, westerly wind differences along the south side of the TP between the SEXP and CTRL experiments enhance water vapor transport, which subsequently converges over the eastern plateau, forming a significant moisture convergence difference (Figures 12a–12c). The moisture divergence and convergence differences between the SEXP and CTRL experiments determine the simulated precipitation differences over the TP from autumn to spring. The intensity of this moisture convergence difference between the SEXP and CTRL experiments exhibits clear seasonal variation, being weaker in winter than in spring and autumn, which is conducive to reducing the positive simulated precipitation bias over TP in winter. In summer, the northward migration of the westerlies shifts the STOFD-induced westerly wind differences from the south side of TP into the plateau interior, increasing moisture inflow over the southern TP (Figure 12d). The significant moisture convergence differences between the SEXP and CTRL experiments over TP in summer create favorable humidity conditions for the increase of simulated precipitation in the SEXP experiment. Supported by the cyclone difference between the SEXP and CTRL experiments over the TP in summer, this enhanced moisture further increases simulated precipitation probability.

Enhanced water vapor transport along the south side of the TP ultimately increases the moisture convergence in the SEC in the SEXP experiment. The moisture convergence difference between the SEXP and CTRL experiments in the SEC displays strong seasonal variability, reaching its minimum intensity in winter and maximum in summer among all seasons (Figure 12). Due to the abundant summer water vapor, the weakest cyclone differences over SEC in summer among all seasons (Figure 10) still generate significant moisture convergence differences between the SEXP and CTRL experiments (Figure 12d). These moisture convergence (divergence) differences between the SEXP and CTRL experiments align well with the precipitation negative (positive) bias in the CTRL

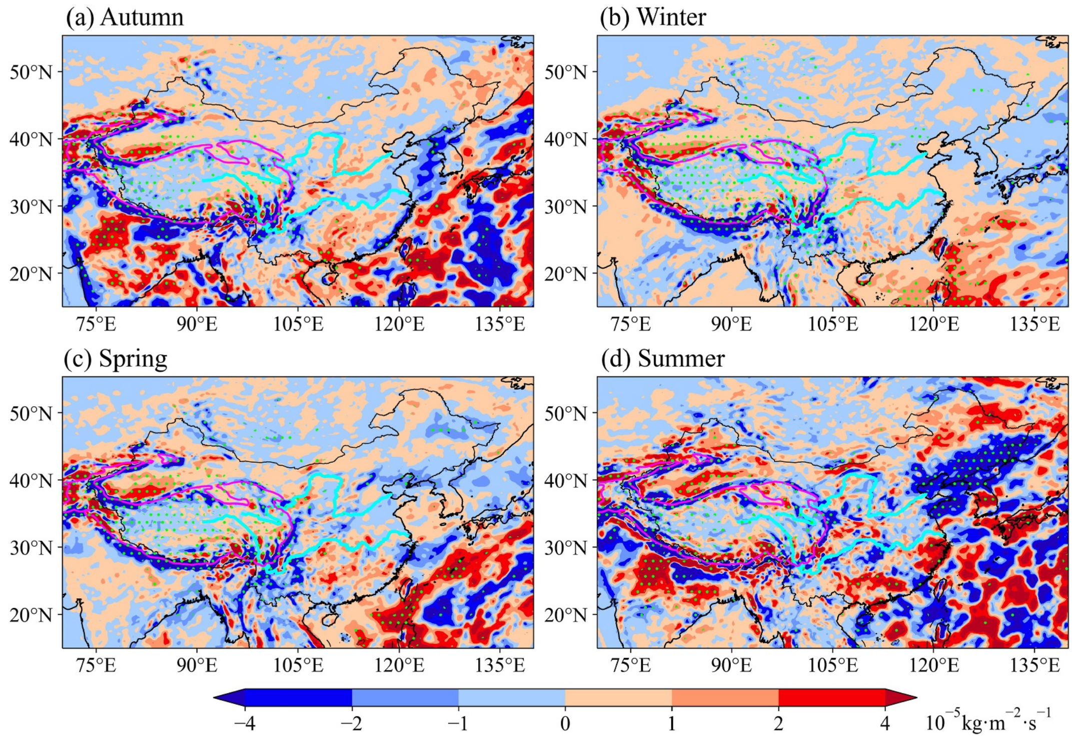

Figure 12. Differences of water vapor flux convergence vertically integrated from surface to 300 hPa (color shadings) between the SEXP and CTRL experiments in each season. Positive values (red shadings) indicate water vapor convergence, calculated by Equation 5. The purple contours (cyan curves) in each subplot indicate the 3,000 m elevation level (the Yangtze River and Yellow River). The green dots denote the differences significant at the 90% confidence level.

experiment, enhancing the accuracy of summer precipitation simulation in the SEXP experiment. In contrast, with the limited water vapor and the southerly location of cyclonic differences (Figure 10b), the moisture convergence differences produced by the STOFD scheme in winter over the SEC are the weakest among all seasons (Figure 12b). Therefore, the improvement of winter precipitation simulation is relatively limited over the SEC.

The effectiveness of STOFD in improving precipitation simulations depends not only on its direct dynamical influences but also on pre-existing model biases in the CTRL experiment. Although STOFD generates similar cyclonic and moisture convergence differences conducive to precipitation increase in autumn and spring, the contrasting initial precipitation biases in the CTRL experiment yield markedly different improvement outcomes (Figures 12a and 12c). In autumn, when the simulation exhibits a negative precipitation bias over the SEC in the CTRL experiment, STOFD-induced significant precipitation increases improve simulation accuracy (Figures 8a and 8e). Conversely, in spring with a positive precipitation bias in the same region, the STOFD-induced increases in simulated precipitation further exacerbate the overestimation, thereby degrading model performance (Figures 8c and 8g).

Under the influence of STOFD-induced anticyclonic differences, the NEC experiences moisture divergence differences throughout all seasons (Figure 12). This effect reaches its maximum intensity during summer when abundant atmospheric moisture enhances the moisture divergence differences between the SEXP and CTRL experiments (Figure 12d). Combined with the descending airflow associated with an anticyclonic difference, these moisture differences produce a substantial reduction in simulated summer precipitation in the SEXP experiment relative to the CTRL experiment. Conversely, autumn demonstrates the weakest moisture divergence differences between the SEXP and CTRL experiments, which, together with relatively weak anticyclonic differences, lead to the limited effect in the SEXP experiment (Figure 12a).

To conclude, the influence of the STOFD scheme exhibits distinct seasonal differences. The effect of STOFD on the westerlies is substantially greater than on the East Asian monsoon, with the most pronounced impacts occurring over the TP and its surroundings, where a westward-oriented drag is generated in all seasons. STOFD obstructs westerlies and water vapor transport across the TP, reducing simulated precipitation over the western plateau in all seasons except summer. According to the quasi-geostrophic approximation of the zonal momentum equation considering STOFD, the STOFD-induced southeasterly wind differences trigger a secondary meridional circulation difference, producing westerly wind differences along both sides of the southeasterly wind differences. The westerly wind differences generated by the STOFD at the south side of the southeasterly wind differences eventually converge over the eastern TP, forming moisture convergence differences there. Downstream propagation of westerly wind differences between the SEXP and CTRL experiments on both sides of the southeasterly wind differences induces cyclonic (anticyclonic) differences and enhances moisture convergence (divergence) over the SEC (NEC), thereby promoting more (less) simulated precipitation over the SEC (NEC) in the SEXP experiment than in the CTRL experiment. The seasonal variations in the precipitation simulation improvement primarily arise from seasonal movement and intensity changes of the westerlies.

During summer, the northward shift and weakening of the westerlies in the CTRL experiment result in corresponding northward migration and intensity reduction of STOFD. This shift confines the southeasterly wind differences generated by the STOFD to the northern TP, confining the development of meridional circulation to that region. Consequently, the westerly wind differences between the SEXP and CTRL experiments emerge over the southern TP, accompanied by a cyclone difference that provides dynamic support for precipitation and enhances moisture convergence into the plateau. The SEC and NEC in the downstream exhibit corresponding variations in the intensity and location of circulation differences and moisture responses that affect the simulated precipitation.

5. Conclusion and Discussion

The seasonality of the effects of the STOFD scheme on model simulation remains inadequately quantified. This study systematically demonstrates that the impacts of the STOFD scheme on simulated 10 m wind and precipitation across China exhibit pronounced seasonal differences, primarily modulated by the seasonal variations in intensity and location of the background westerlies.

Systematic evaluation reveals that the efficacy of the STOFD scheme in improving 10 m wind simulations exhibits strong seasonality, with the most substantial improvement occurring in winter and the weakest in summer among all seasons. The magnitude of improvement in all seasons is positively correlated with micro-scale terrain complexity. The direct influence of the STOFD scheme on near-surface circulation at different pressure levels is similar to that of 10 m wind across all seasons. For simulated precipitation, STOFD most effectively reduces the positive bias over the TP in winter, improving the RMSE by 9.69%. Over the SEC and NEC, STOFD yields the most significant improvement in precipitation simulation during summer, with RMSE improvements of 6.45% and 33.11%, respectively.

The physical mechanism centers on the effect of STOFD on prevailing westerlies (Figure 13). By impeding the background westerlies, STOFD generates southeasterly wind differences, exciting a secondary meridional circulation difference. The secondary meridional circulation difference leads to a dipole pressure difference that produces westerly wind differences along both the north and south sides of the southeasterly wind differences. The resulting downstream effects are characterized by cyclonic differences coupled with moisture convergence differences over the SEC, and anticyclonic differences accompanied by moisture divergence differences over the NEC. This chain of processes creates favorable dynamic and moisture conditions for simulated precipitation improvement. Improvements in 10 m wind simulation arise from both the direct effects and the circulation adjustment of STOFD.

Seasonal differences in the impacts of the STOFD scheme are primarily driven by combined variations in the intensity and north-south migration of the background westerlies in different seasons. The strong winter westerlies amplify the STOFD's effects, the resulting circulation adjustments, resulting in the most significant improvement in 10 m wind. The northward-shifted and weakened westerlies in summer confine and redirect the STOFD-induced perturbations, leading to a distinct spatial pattern of 10 m wind and precipitation differences compared to other seasons.

Consistent with previous studies, this study confirms that STOFD significantly influences simulated precipitation in eastern China, further emphasizing the importance of the remote effects of STOFD originating over TP and its surroundings (Gu et al., 2023a; Y. Zhou et al., 2024). This study also elucidates how STOFD-induced

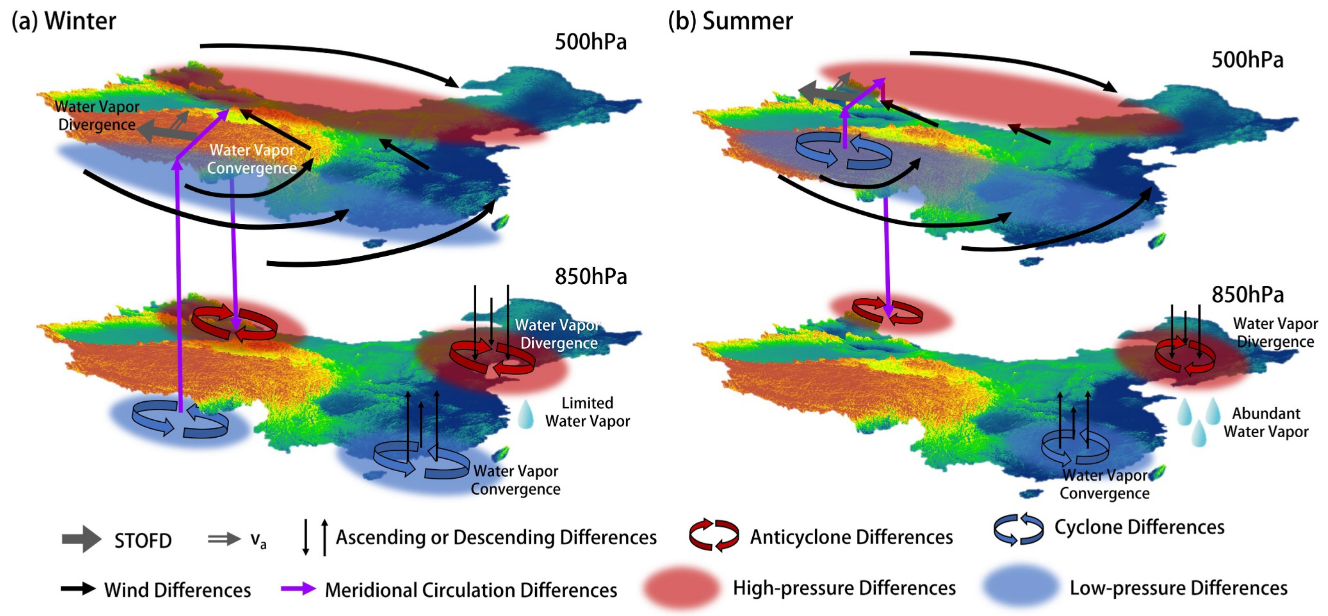

Figure 13. Schematic diagram of the seasonal difference in the influence of sub-grid turbulent orographic form drag (STOFD) on simulated atmospheric circulation and precipitation. v_a represents the ageostrophic southerly component induced by the STOFD scheme. Only the summer and winter versions are presented as representative mechanisms.

deceleration of westerlies enhances simulated spring precipitation in the SEC. Similarly, R. Li et al. (2023) demonstrated that orographic gravity wave drag enhances moisture transported by the southwesterly monsoon through a parallel mechanism, intensifying spring rainfall in the same region. This indicates that distinct orographic drag parameterizations can produce analogous regional climate impacts through similar dynamical mechanisms.

This study primarily examines the seasonal differences in the influence of the STOFD scheme on near-surface winds and precipitation. Notably, the implementation of the STOFD scheme does not consistently reduce simulation biases across all seasons, particularly for precipitation. The application of other dynamic and thermal effects of terrain is also necessary to reduce the deviations. Furthermore, while this paper focuses on the dynamic effects of STOFD, its impact on the seasonal thermal implications of heat flux transport and surface radiative warming induced by precipitation remains unexplored. Comprehensive mechanism understanding requires a systematic examination of the thermal and other dynamic effects of sub-grid terrain, including their indirect interactions and feedback.

Several limitations are noted. Due to the lack of mesoscale sub-grid orography parameterization in RegCM, the diagnosed seasonal sensitivity of the STOFD scheme may implicitly include contributions from unresolved mesoscale orographic drag. Further evaluation within a multi-scale terrain drag framework is therefore needed. The current analysis shows that direct STOFD forcing indeed induces a secondary meridional circulation difference. However, the secondary meridional circulation difference may also be influenced by other factors, such as nonlinear model feedback, which the current analysis is unable to distinguish. By comparing the patterns of difference between the SEXP and CTRL experiments with the STOFD distribution, the present analysis distinguishes the direct and indirect effects of STOFD, but this approach provides only a partial separation. The more rigorous disentanglement would require additional experiments and analysis, which is deferred to future work. The conclusions are derived from a specific model (RegCM4) and regional domain, and the generalizability of STOFD effects across different modeling systems requires further validation. The current B04 scheme also has inherent simplifications, such as assuming isotropic terrain and employing a topographic spectral function based on 30″ (~1 km) resolution elevation data. To ultimately improve the scheme's accuracy and applicability across diverse geographical contexts, future refinements should incorporate topographic anisotropy and employ high-resolution elevation data sets to reselect the terrain filtering range, thereby obtaining a more accurate small-scale orographic spectrum.

Conflict of Interest

The authors declare no conflicts of interest relevant to this study.

Availability Statement

The data sets utilized in this study include: the Asian Precipitation-Highly-Resolved Observational Data Integration Towards Evaluation daily precipitation product (0.25° × 0.25°; APHRODITE, 2012); the fifth generation ECMWF atmospheric reanalysis of the global climate (ERA5) with a horizontal resolution of 0.25° × 0.25° (ECMWF, 2020); the NOAA Optimum Interpolation Sea Surface Temperature (OISST) data set (1° × 1°; NOAA, 2002); the ERA-Interim reanalysis (1.5° × 1.5°; ECMWF, 2011); the European Space Agency (ESA) Climate Change Initiative (CCI) Essential Climate Variable (ECV) Surface Soil Moisture and Combined Product (0.25° × 0.25°; Dorigo et al., 2021); and the Global Multi-resolution Terrain Elevation Data (GMTED; 30″ × 30″; Danielson & Gesch, 2011), obtained from the U.S. Geological Survey (USGS). Regional climate simulations were performed using RegCM4 (ICTP, 2016) and a modified version incorporating the STOFD parameterization scheme (Gu et al., 2023b).

Acknowledgments

This study is supported by the following sources: the National Natural Science Foundation of China (Grant 42375157), the National Key R&D Program of China (Grant 2022YFC3080500), the Beijige Open Research Fund (Grant BJG202403), the China Postdoctoral Science Foundation (2025M780281), and the Postdoctoral Fellowship Program of CPSF (GZC20260160). We also gratefully acknowledge the High Performance Computing Center of Nanjing University for providing computational resources.

References

Andrade Cardoso, A., Porfírio da Rocha, R., Simões Reboita, M., Machado Crespo, N., Traversi de Cai Conrado, E., & Vidale, P. L. (2025). Performance of the medium and high horizontal resolution models from HighResMIP-CMIP6 in simulating synoptic-scale cyclones over South America. *Climate Dynamics*, *63*(1), 83. https://doi.org/10.1007/s00382-024-07579-3

APHRODITE. (2012). A long-term daily gridded precipitation dataset for Asia based on a dense network of rain gauges [Datasets]. *APHRODITE*. Retrieved from http://aphrodite.st.hirosaki-u.ac.jp/download/

Asakereh, H., & Jahedi, A. (2025). Long-term changes in the speed and direction of westerlies in the mid-latitudes of the northern hemisphere (MLNH). *Acta Geophysica*, *73*(4), 1–21. https://doi.org/10.1007/s11600-024-01525-x

Belcher, S. E., Newley, T. M. J., & Hunt, J. C. R. (1993). The drag on an undulating surface induced by the flow of a turbulent boundary layer. *Journal of Fluid Mechanics*, *249*, 557–596. https://doi.org/10.1017/S0022112093001296

Beljaars, A. C. M., Brown, A. R., & Wood, N. (2004). A new parametrization of turbulent orographic form drag. *Quarterly Journal of the Royal Meteorological Society*, *130*(599), 1327–1347. https://doi.org/10.1256/qj.03.73

Cai, S., Huang, A., Zhu, K., Guo, W., Wu, Y., & Gu, C. (2023). The forecast skill of the summer precipitation over Tibetan plateau improved by the adoption of a 3D sub-grid terrain solar radiative effect scheme in a convection-permitting model. *Journal of Geophysical Research: Atmospheres*, *128*(11), e2022JD038105. https://doi.org/10.1029/2022JD038105

Cannon, F., Carvalho, L. M., Jones, C., Norris, J., Bookhagen, B., & Kiladis, G. N. (2017). Effects of topographic smoothing on the simulation of winter precipitation in high Mountain Asia. *Journal of Geophysical Research: Atmospheres*, *122*(3), 1456–1474. https://doi.org/10.1002/2016JD026038

Choi, H. J., Choi, S. J., Koo, M. S., Kim, J. E., Kwon, Y. C., & Hong, S. Y. (2017). Effects of parameterized orographic drag on weather forecasting and simulated climatology over East Asia during boreal summer. *Journal of Geophysical Research: Atmospheres*, *122*(20), 10–669. https://doi.org/10.1002/2017JD026696

Curio, J., & Scherer, D. (2016). Seasonality and spatial variability of dynamic precipitation controls on the Tibetan Plateau. *Earth System Dynamics*, *7*(3), 767–782. https://doi.org/10.5194/esd-7-767-2016

Danielson, J. J., & Gesch, D. B. (2011). Global multi-resolution terrain elevation data 2010 (GMTED2010) [Datasets]. *USGS*. https://doi.org/10.3133/ofr20111073

Dee, D. P., Uppala, S. M., Simmons, A. J., Berrisford, P., Poli, P., Kobayashi, S., et al. (2011). The ERA-interim reanalysis: Configuration and performance of the data assimilation system. *Quarterly Journal of the Royal Meteorological Society*, *137*(656), 553–597. https://doi.org/10.1002/qj.828

Dickinson, R. E., Errico, R. M., Giorgi, F., & Bates, G. T. (1989). A regional climate model for the western United States. *Climatic Change*, *15*(3), 383–422. https://doi.org/10.1007/BF00240465

Dixit, A., Sahany, S., Mishra, S. K., & Mesquita, M. D. (2023). Seasonal dependent suitability of physical parameterizations to simulate precipitation over the Himalayan headwater. *Scientific Reports*, *13*(1), 4756. https://doi.org/10.1038/s41598-023-31353-w

Dorigo, W., Preimesberger, W., Moesinger, L., Pasik, A., Scanlon, T., Hahn, S., et al. (2021). ESA soil moisture climate change initiative (Soil_Moisture_cci): COMBINED product. Version 06.1 [Dataset]. *NERC EDS Centre for Environmental Data Analysis*. Retrieved from https://catalogue.ceda.ac.uk/uuid/43d73291472444e6b9c2d2420dbad7d6

ECMWF. (2011). The ECMWF reanalysis-interim (ERA-Interim) [Dataset]. *ECMWF*. Retrieved from https://www.ecmwf.int/en/forecasts/dataset/ecmwf-reanalysis-interim

ECMWF. (2020). The ECMWF reanalysis version 5 (ERA5) [Dataset]. *ECMWF*. Retrieved from https://www.ecmwf.int/en/forecasts/dataset/ecmwf-reanalysis-v5

Elvidge, A. D., Sandu, I., Wedi, N., Vosper, S. B., Zadra, A., Boussetta, S., et al. (2019). Uncertainty in the representation of orography in weather and climate models and implications for parameterized drag. *Journal of Advances in Modeling Earth Systems*, *11*(8), 2567–2585. https://doi.org/10.1029/2019MS001661

Gao, X., & Giorgi, F. (2017). Use of the RegCM system over East Asia: Review and perspectives. *Engineering*, *3*(5), 766–772. https://doi.org/10.1016/J.ENG.2017.05.019

Giorgi, F., & Marinucci, M. R. (1991). Validation of a regional atmospheric model over Europe: Sensitivity of wintertime and summertime simulations to selected physics parametrizations and lower boundary conditions. *Quarterly Journal of the Royal Meteorological Society*, *117*(502), 1171–1206. https://doi.org/10.1002/qj.49711750204

Gu, C., Huang, A., Li, X., Yang, B., Zhou, X., & Wu, Y. (2023a). Impact of sub-grid turbulent orographic form drag on the summer monsoon precipitation simulation over China. *Journal of Geophysical Research: Atmospheres*, *128*(20), e2023JD039113. https://doi.org/10.1029/2023jd039113

Gu, C., Huang, A., Li, X., Yang, B., Zhou, X., & Wu, Y. (2023b). The source codes of sub-grid turbulent orographic form drag parameterization scheme suitable for the regional climate model version 4.5.0 (RegCM4) [Software]. *Zenodo*. https://doi.org/10.5281/zenodo.8077329

Gu, C., Huang, A., Zhang, Y., Yang, B., Cai, S., Xu, X., et al. (2022). The wet bias of RegCM4 over Tibet Plateau in summer reduced by adopting the 3D sub-grid terrain solar radiative effect parameterization scheme. *Journal of Geophysical Research: Atmospheres*, *127*(21), e2022JD037434. https://doi.org/10.1029/2022JD037434

Holtslag, A. A. M., De Bruijn, E. I. F., & Pan, H.-L. (1990). A high resolution air mass transformation model for short-range weather forecasting. *Monthly Weather Review*, *118*(8), 1561–1575. https://doi.org/10.1175/1520-0493(1990)118<1561:Ahramt>2.0.Co;2

Huang, H., Su, J., & Wang, F. Y. (2024). The potential of low-altitude airspace: The future of urban air transportation. *IEEE Transactions on Intelligent Vehicles*, *9*(8), 5250–5254. https://doi.org/10.1109/TIV.2024.3483889

ICTP. (2016). The regional climate model version 4.5.0 (RegCM4) [Software]. *Zenodo*. https://doi.org/10.5281/zenodo.8077329

Ilyas, M., Noack, B. R., Hu, G., Xiong, H., Gao, N., Khan, A., & Yang, Y. (2025). Drone anemometry of atmospheric winds—A review. *Physics of Fluids*, *37*(6), 061302. https://doi.org/10.1063/5.0259355

Jo, K. R., Kim, S. R., Pak, K. S., Kim, H. C., & Ham, Y. S. (2024). Impact of convective and land surface parameterization schemes on the simulation of surface temperature and precipitation using RegCM4. 7 during summer period over the DPR Korea. *Pure and Applied Geophysics*, *181*(8), 2703–2715. https://doi.org/10.1007/s00024-024-03490-4

Kain, J. S., & Fritsch, J. M. (1990). A one-dimensional entraining/detraining plume model and its application in convective parameterization. *Journal of the Atmospheric Sciences*, *47*(23), 2784–2802. https://doi.org/10.1175/1520-0469(1990)047<2784:AODEPM>2.0.CO;2

Kiehl, J. T., Hack, J. J., Bonan, G. B., Boville, B. A., Williamson, D. L., & Rasch, P. J. (1998). The national center for atmospheric research community climate model: CCM3. *Journal of Climate*, *11*(6), 1131–1149. https://doi.org/10.1175/1520-0442(1998)011<1131:Tncfar>2.0.Co;2

Koo, M. S., Choi, H. J., & Han, J. Y. (2018). A parameterization of turbulent-scale and mesoscale orographic drag in a global atmospheric model. *Journal of Geophysical Research: Atmospheres*, *123*(16), 8400–8417. https://doi.org/10.1029/2017JD028176

Lee, L., Pang, B., & Low, K. H. (2022). Environmental data analytics for safe drone operations in low-altitude urban environments. In *AIAA aviation 2022 forum*. https://doi.org/10.2514/6.2022-3405

Li, J., Lu, C., Chen, J., Zhou, X., Yang, K., Li, J., et al. (2024). The influence of complex terrain on cloud and precipitation on the foot and slope of the southeastern Tibetan Plateau. *Climate Dynamics*, *62*(5), 3143–3163. https://doi.org/10.1007/s00382-023-07056-3

Li, R., Xu, X., Xu, X., Shepherd, T. G., & Wang, Y. (2023). Importance of orographic gravity waves over the Tibetan Plateau on the spring rainfall in East Asia. *Science China Earth Sciences*, *66*(11), 2594–2602. https://doi.org/10.1007/s11430-023-1204-6

Liu, Y., Giorgi, F., & Washington, W. M. (1994). Simulation of summer monsoon climate over East Asia with an NCAR regional climate model. *Monthly Weather Review*, *122*(10), 2331–2348. https://doi.org/10.1175/1520-0493(1994)122<2331:SOSMCO>2.0.CO;2

Lu, C., Huang, G., & Wang, X. (2019). Projected changes in temperature, precipitation, and their extremes over China through the RegCM. *Climate Dynamics*, *53*(9), 5859–5880. https://doi.org/10.1007/s00382-019-04899-7

Namdev, P., Srivastava, P., Sharan, M., & Mishra, S. K. (2024). An update to WRF surface layer parameterization over an Indian region. *Dynamics of Atmospheres and Oceans*, *105*, 101414. https://doi.org/10.1016/j.dynatmoce.2023.101414

NOAA. (2002). The weekly NOAA optimum interpolation sea surface temperature (OISST) [Dataset]. *National Oceanic and Atmospheric Administration*. Retrieved from https://psl.noaa.gov/data/gridded/data.noaa.oisst.v2.html

Oleson, K., Lawrence, D., Bonan, G., Drewniak, B., Huang, M., Koven, C., et al. (2010). Technical description of version 4.5 of the community land model (CLM). *NCAR Tech. Notes (NCAR/TN-478+ STR)*.

Pal, J. S., Small, E. E., & Eltahir, E. A. B. (2000). Simulation of regional-scale water and energy budgets: Representation of subgrid cloud and precipitation processes within RegCM. *Journal of Geophysical Research*, *105*(D24), 29579–29594. https://doi.org/10.1029/2000JD900415

Park, H., Hwang, J., Cha, D. H., Lee, M. I., Song, C. K., Kim, J., et al. (2024). Does a scale-aware convective parameterization scheme improve the simulation of heavy rainfall events? *Journal of Geophysical Research: Atmospheres*, *129*(7), e2023JD039407. https://doi.org/10.1029/2023JD039407

Qin, S., Zhan, D., Geng, D., Peng, W., Tian, G., Shi, Y., et al. (2025). Modeling multivariable high-resolution 3D urban microclimate using localized Fourier neural operator. *Building and Environment*, *273*, 112668. https://doi.org/10.1016/j.buildenv.2025.112668

Reynolds, R. W., Rayner, N. A., Smith, T. M., Stokes, D. C., & Wang, W. (2002). An improved in situ and satellite SST analysis for climate. *Journal of Climate*, *15*(13), 1609–1625. https://doi.org/10.1175/1520-0442(2002)015<1609:AIISAS>2.0.CO;2

Sandu, I., Bechtold, P., Beljaars, A., Bozzo, A., Pithan, F., Shepherd, T. G., & Zadra, A. (2016). Impacts of parameterized orographic drag on the northern hemisphere winter circulation. *Journal of Advances in Modeling Earth Systems*, *8*(1), 196–211. https://doi.org/10.1002/2015MS000564

Sandu, I., Niekerk, A. V., Shepherd, T. G., Vosper, S. B., & Svensson, G. (2019). Impacts of orography on large-scale atmospheric circulation. *Climate Atmospheric Science*, *2*(10), 1–8. https://doi.org/10.1038/s41612-019-0065-9

Student. (1908). The probable error of a mean. *Biometrika*, *6*(1), 1–25. https://doi.org/10.2307/2331554

Taylor, K. E. (2001). Summarizing multiple aspects of model performance in a single diagram. *Journal of Geophysical Research*, *106*(D7), 7183–7192. https://doi.org/10.1029/2000JD900719

Tiedtke, M. (1996). An extension of cloud-radiation parameterization in the ECMWF model: The representation of subgrid-scale variations of optical depth. *Monthly Weather Review*, *124*(4), 745–750. https://doi.org/10.1175/1520-0493(1996)124<0745:Aeocrp>2.0.Co;2

van Niekerk, A., Shepherd, T. G., Vosper, S. B., & Webster, S. (2016). Sensitivity of resolved and parametrized surface drag to changes in resolution and parametrization. *Quarterly Journal of the Royal Meteorological Society*, *142*(699), 2300–2313. https://doi.org/10.1002/qj.2821

Wang, Y., Wang, L., Feng, J., Song, Z., Wu, Q., & Cheng, H. (2023). A statistical description method of global sub-grid topography for numerical models. *Climate Dynamics*, *60*(7), 2547–2561. https://doi.org/10.1007/s00382-022-06447-2

Wang, Y., & Wu, J. (2022). Overview of the application of orographic data in numerical weather prediction in complex orographic areas. *Advances in Meteorology*, *2022*(1), 1279625. https://doi.org/10.1155/2022/1279625

Wang, Y., Yang, K., Zhou, X., Chen, D., Lu, H., Ouyang, L., et al. (2020). Synergy of orographic drag parameterization and high resolution greatly reduces biases of WRF-simulated precipitation in central Himalaya. *Climate Dynamics*, *54*(3), 1729–1740. https://doi.org/10.1007/s00382-019-05080-w

World Meteorological Organization. (2015). Seamless prediction of the Earth system: From minutes to months (WMO-No. 1156). Retrieved from https://library.wmo.int/records/item/34163-seamless-prediction-of-the-earth-system-from-minutes-to-months

Wu, Y., Huang, A., Huang, D., Chen, F., Yang, B., Zhou, Y., et al. (2018). Diurnal variations of summer precipitation over the regions east to Tibetan Plateau. *Climate Dynamics*, *51*(11), 4287–4307. https://doi.org/10.1007/s00382-017-4042-x

Xu, X., Li, M., Zhong, S., & Wang, Y. (2023). Impact of parameterized topographic drag on a simulated Northeast China cold vortex. *Journal of Geophysical Research: Atmospheres*, *128*(3), e2022JD037664. https://doi.org/10.1029/2022JD037664

Xue, H., & Shen, X. (2023). A turbulent orographic form drag scheme accounting for anisotropy and orientation for kilometer-to subkilometer-scale models. *Quarterly Journal of the Royal Meteorological Society*, *149*(755), 2527–2549. https://doi.org/10.1002/qj.4519

Xue, H., Zhou, X., Luo, Y., & Yin, J. (2021). Impact of parameterizing the turbulent orographic form drag on convection-permitting simulations of winds and precipitation over South China during the 2019 pre-summer rainy season. *Atmospheric Research*, *263*, 105814. https://doi.org/10.1016/j.atmosres.2021.105814

Yatagai, A., Kamiguchi, K., Arakawa, O., Hamada, A., Yasutomi, N., & Kitoh, A. (2012). APHRODITE: Constructing a long-term daily gridded precipitation dataset for Asia based on a dense network of rain gauges. *Bulletin of the American Meteorological Society*, *93*(9), 1401–1415. https://doi.org/10.1175/bams-d-11-00122.1

Yihui, D., & Chan, J. C. (2005). The East Asian summer monsoon: An overview. *Meteorology and Atmospheric Physics*, *89*(1), 117–142. https://doi.org/10.1007/s00703-005-0125-z

Zeng, X., Zhao, M., & Dickinson, R. E. (1998). Intercomparison of bulk aerodynamic algorithms for the computation of sea surface fluxes using TOGA COARE and TAO data. *Journal of Climate*, *11*(10), 2628–2644. https://doi.org/10.1175/1520-0442(1998)011<2628:Iobaaf>2.0.Co;2

Zhou, X., Beljaars, A., Wang, Y., Huang, B., Lin, C., Chen, Y., & Wu, H. (2017). Evaluation of WRF simulations with different selections of subgrid orographic drag over the Tibetan Plateau. *Journal of Geophysical Research: Atmospheres*, *122*(18), 9759–9772. https://doi.org/10.1002/2017JD027212

Zhou, X., Yang, K., Beljaars, A., Li, H., Lin, C., Huang, B., & Wang, Y. (2019). Dynamical impact of parameterized turbulent orographic form drag on the simulation of winter precipitation over the western Tibetan Plateau. *Climate Dynamics*, *53*(1–2), 707–720. https://doi.org/10.1007/s00382-019-04628-0

Zhou, X., Yang, K., & Wang, Y. (2018). Implementation of a turbulent orographic form drag scheme in WRF and its application to the Tibetan Plateau. *Climate Dynamics*, *50*(7–8), 2443–2455. https://doi.org/10.1007/s00382-017-3677-y

Zhou, Y., Huang, A., Li, X., Gu, C., & Wu, Y. (2024). Local and remote effects of the sub-grid turbulent orographic form drag on the summer monsoon precipitation over Eastern China. *Journal of Geophysical Research: Atmospheres*, *129*(20), e2024JD041173. https://doi.org/10.1029/2024JD041173

Zuo, X., & Wu, G. (2025). Evaluation of different sub-grid orographic drag schemes on typhoon precipitation in Northeast China in the weather research and forecasting model. *Quarterly Journal of the Royal Meteorological Society*, *151*(773), e70004. https://doi.org/10.1002/qj.70004